Chapter 5

Tropospheric Tomography

The application of tomography to the troposphere presents larger technical difficulties than its application to the ionosphere. They are mainly due to two reasons: first, the observable is the slant wet delay, which requires a refinement in the GPS data processing; second, local dense networks are required. It is therefore necessary to carry a finer analysis than in the ionospheric case in order to validate the results.

In this chapter we extensively use simulations to determine system parameters such as the resolution or the impact of noise, and then we apply simulated realistic distributions of refractivity, to determine the feasibility of tomography; in the simulations, different network geometries have been considered.

Finally, we use experimental GPS data tracked at the local networks in Kilauea (the February 1997 configuration) and at Onsala (the REGINA experiment in August 1998) to generate 4D tomographic maps of wet refractivity. Radiosonde data, simulations with the numerical weather model NCAR Mesoscale Model (MM5*), satellite data from the US National Oceanic and Atmospheric Administration (NOAA) and data and analysis from the European Center for Medium-Range Weather Forecast (ECMWF) have been used to evaluate our results. We have included Appendix B to provide a basic reference of meteorological magnitudes and concepts which are used in this chapter.

5.1 Tropospheric tomography equations

In Section 2.3.2.2 the effect of the neutral atmosphere in the GPS signal was described and related to the neutral refractivity (see Equation 2.17). Furthermore, it was shown in Equation 2.26 how the atmospheric delay was modeled as a zenith component plus horizontal gradients. Hydrostatic components can be characterized from surface measurements and are well modeled. It is therefore interesting to obtain the spatio-temporal description of the wet

*http://www.mmm.ucar.edu/mm5/mm5-home.html

refractivity. To this end, we need to form the slant wet delays (SWD).

5.1.1 The observations equations: the slant wet delays

The output of the regular GPS data processing are the time series of the total zenith component and the total gradients. In order to form the SWD, we need to remove the hydrostatic zenith delays and horizontal gradients from the solution using external measurements or analysis [†]. The hydrostatic zenith component can be removed, as shown in Chapter 2, using surface pressure measurements; currently these have a 1 mbar precision or better, which corresponds to 2 mm in zenith delay.

The gradient parameter $\vec{L}^G(t)$ in Equation 2.22 has units of excess path length and is a site-dependent parameter defined as ([36], and see Appendix A)

$$\vec{L}^G(t) = 10^{-6} \int_0^\infty dz z \vec{\psi}(z,t), \tag{5.1}$$

where $\vec{\psi}(z,t) = \nabla_{\vec{\rho}} N(\vec{\rho}, z, t)|_{\vec{\rho}=0}$ is the horizontal gradient of the refractivity, $\vec{\rho}$ is the horizontal displacement vector, and z is the height above the surface. However, as shown in [40] and [72][‡] a gradient of the zenith component can be computed as

$$\vec{G}(t) = 10^{-6} \int_0^\infty dz \vec{\psi}(z,t), \tag{5.2}$$

and has units of excess path length per unit distance. The relationship between $\vec{L}^G(t)$ and $\vec{G}(t)$ for the hydrostatic case can be obtained by assuming an exponential law for N_h leading to $\vec{L}_h^G(t) = H\vec{G}_h(t)$, where H is the scale height (see Appendix A). Thus, the hydrostatic gradients can be removed by estimating the ZHD at each site, compute $\vec{G}_h$ and then obtain $\vec{L}_h^G$ (another approach is described in [29] where they are considered to be constant over periods of 12 hours and hence removed by averaging the gradient solution over that period and demeaning it). The removal of hydrostatic gradients is a key step in the processing, because it has a direct impact on the interpretation of the 4D fields retrieved with tomography: if the hydrostatic gradients are present in the observables that enter in the tomographic inversion process, the resulting field will reflect these gradients, not only the water vapor distribution.

Once the hydrostatic components have been removed, the SWD are formed by mapping the zenith and gradient time-series solutions to the directions of the rays and adding the post-fit residuals to each measurement. This recreates the individual slant delay measurement. Post-fit residuals may include unmodeled effects such as the 3D distribution of the water vapor (particularly elevations below 10^o) as well as unmodeled noise. In fact, the increased scatter

[†] Note that they can also be removed prior to any data processing

[‡] We will follow the notation of [40] because the results there presented will be used for a comparative analysis

of the residuals at low elevations reveals a possible deficiency in the mapping functions. The non-inclusion of the residuals would drag the angle dependencies of the wet delays described by the mapping functions into the tomographic solution. Moreover, the decomposition of the refractivity into a zenith component plus a horizontal gradient is a first- order approximation, which may fail to describe some refractivity structures ([73]). The addition of the post-fit residuals, however, also means the addition of multipath noise, clock errors, coordinate errors, and phase noise to the observables.

As described in Chapter 2, each SWD is an observation (y) and we can construct a linear system by arranging all the observations and modeling in matrix form $\mathbf{y} = \mathbf{Ax}$ (Equation 3.11).

Note that our tomographic approach does not consider the bending of the ray in the atmosphere and, therefore, the mapping function formed due to the discretization of the atmosphere into uniform layers (basically a 1/sin(e) function) is less accurate than other mapping functions that are corrected by the bending effect, such as the Niell mapping function ([38]). Further improvements should take into account this effect. In a differential approach this fact is less important.

5.1.1.1 Analysis of errors in the SWD calculation

We have mentioned two sources of errors when describing the formation of the SWD: the remaining hydrostatic components and the addition of noise via the post-fit residues.

Let us first consider that zenith hydrostatic delays are removed using surface pressure measurements with a 1 mbar accuracy and that hydrostatic gradients are not removed. In such a case, one would be dealing with *pseudo-wet delays* as observables and one would be retrieving the *pseudo-wet refractivity* $\hat{N}$ field, which to first order can be written as

$$\begin{aligned}\hat{N}(z,\vec{\rho},t) = N_w(z,t) + \vec{\psi}_w(z,t)\cdot\vec{\rho} + \Delta N_{oh}(z,t) \\ + \vec{\psi}_h(z,t)\cdot\vec{\rho},\end{aligned} \tag{5.3}$$

where $\Delta N_{oh}(z,t)$ stands for the refractivity error due to the 1 mbar accuracy of the surface pressure measurements, $\vec{\psi}_h(z,t)$ is the hydrostatic refractivity gradient and $\vec{\psi}_w(z,t)$ is the wet refractivity gradient. Therefore, if one considers this to be the real wet refractivity, the total error is:

$$\Delta N(z,\vec{\rho},t) = \Delta N_{oh}(z,t) + \vec{\psi}_h(z,t)\cdot\vec{\rho}. \tag{5.4}$$

The value of $\Delta N_{oh}(z,t)$ introduces a random error in the field of about 0.1% in the surface value of N_h (N_h is proportional to P and current barometers have a precision better than 1

mbar, thus $\Delta P/P \leq 0.001$ and $\Delta N_{oh}/N_{oh} \leq 0.001$). The unremoved hydrostatic gradient, $\vec{\psi}_h(z,t)$, on the other hand, appears in the solution as a systematic tilt. The importance of this tilt is relative to the magnitude of the wet gradient.

Let us now consider the noise added via the post-fit residues and how they map in the observables. The phase noise is considered in the GOA II GPS data processing by assigning a 2 mm sigma value to the observations. This yields a formal variance of the zenith wet delay estimation of about 0.5 cm ($\sigma \approx$1 cm for an elevation of 30^o). This uncertainty is included in the tomographic processing as σ_y value. Coordinate errors ($\approx$ 2 mm), clock errors and multipath at each station, included in the post-fit residues, are uncorrelated from one station to another since we use a Precise Point Positioning strategy; the combination of all rays in the tomographic solution will also remove the uncorrelated noise from the solution. In contrast, mapping functions mismodeling actually removes signal from the observables. We can therefore conclude that the addition of the post-fit residuals is needed and that the added noise is usually below the formal uncertainty of the observable and also uncorrelated with the wet troposphere structure. A time-dependency of post-fit residuals reveals a possible mismodeling in the GPS data processing of effects such as the non-inclusion of antenna phase pattern or ocean loading.

5.1.2 The equations of constraints

Having defined the observable for the tropospheric tomography and how to form $\mathbf{y} = \mathbf{Ax}$, attention must be drawn to the definition of the constraints, $\mathbf{l} = \mathbf{Bx}$ (Equation 3.12). The problem in the troposphere, when compared with the ionospheric case, is that the scales are much smaller: the region under study is much smaller (400 km^2 or less) because of the high spatial variability of water vapor. We therefore need local tracking networks of that size. The vertical resolution, on the other hand, is mostly determined by the distribution of the stations (it is difficult to obtain an occultation that senses down to the surface and in the small area where the local tomography is to be carried out; furthermore, only with a dense constellation of LEO sounders could it be expected to have several of such measurements in the area under analysis within some hours). Finally, the larger water vapor amounts are generally confined to the first 2-3 km in height; if we want to describe the vertical distribution of water vapor, we must have a resolution considerably smaller than 2 km. The system is foreseen to be highly undetermined and constraints will be needed.

In order not to loose generality and since there is no reliable a priori model of the structure of the water vapor in time and space, we only use smoothing constraints, with little physics in them. We have found that we need horizontal constraints, vertical constraints and, finally, a

boundary constraint setting the solution to zero at altitudes above 15 km. This can be seen in the evolution of the eigenvalues: we discussed in Section 3.1.2.3 of Chapter 3 that constraints were needed in the minimum amount to make the eigenvalues of the matrix $\mathbf{S}^T \left(\mathbf{C}_{\hat{y}}\right)^{-1} \mathbf{S}$ (see Equation 3.17 in Chapter 3) to be above a cut-off value set by the noise-to-variance ratio. The weight of the constraints need to be tuned for each geometry, since the eigenvalues depend on the ray distribution. If we consider as an example the geometry of the ground network of Hawaii 1997 (to be described later) and the observations at 300 s rate during one complete day, and then plot the evolution of the eigenvalues of such system when successively adding the horizontal, vertical and boundary constraints (see Figure 5.1) it is clear that the three types of constraints are needed. Of course, a similar non-zero eigenvalues situation could have been found by imposing very strong smoothing, but then the solution would be an almost uniform field, thus producing high residuals (very poor resolution). As it is discussed in [42], the trade-off between resolution and variance (which in fact, inversely depends on the eigenvalues) does not allow to have small variance with high resolution and it is always best to use the finest discretization possible. To impose strong smoothing constraints, is equivalent to use a more coarse discretization.

5.2 Results with simulated data

5.2.1 Characterization of the system: Resolution and Noise

It was described in Chapter 3 the necessity to introduce a cut-off value for the eigenvalues of the matrix to be inverted to damp the solution noise. Now, let us compute this cut-off value for the wet tropospheric tomography. The water vapor content is characterized by the mixing ratio $r = \rho_w/\rho_d$ expressed in g/kg (ρ_d is the dry air density and ρ_w is the water vapor density; see Appendix B for further meteorological definitions, which will be used throughout this chapter). Following [20] and [74], at mid-latitudes the relative error in current estimations of r is $\Delta r/r = 10\%$, and a typical value at the Earth's surface is $r \approx 5$ g/kg, and hence a typical uncertainty of $\Delta r \approx 0.5$ g/kg. Using standard surface values for the rest of parameters, and the expression (r in g/kg, N_w in mm/km, P in mbar, T in Kelvin)

$$N_w = \frac{377.6}{0.622} r \frac{P}{T^2}, \tag{5.5}$$

we obtain an uncertainty of $\Delta N_w = \sigma_x \approx 3.5$ mm/km at zero height. Taking $\sigma_y = 10$ mm, as we discussed in a previous section, the cut-off value for the singular values of $\mathbf{S}$ is $\nu > 2.8$ km, which implies a cut-off value of $w = \nu^2 > 8.1$ km^2 for the inversion of $\mathbf{S}^T \left(\mathbf{C}_{\hat{y}}\right)^{-1} \mathbf{S}$. The minimum effective length represented by ν=2.8 km implies (see Chapter 3) that the minimum

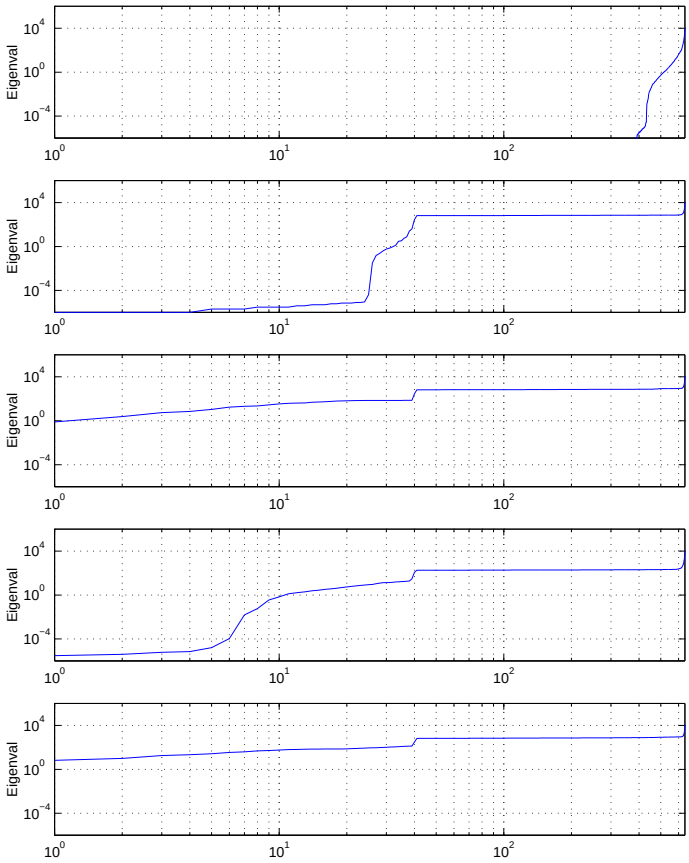

Figure 5.1: Evolution of eigenvalues without any constraints (top), with horizontal constraints, horizontal and (strong) vertical, horizontal and boundary and with all constraints, from top to bottom . The case with strong vertical smoothing shows that when the constraints have a too high value the eigenvalue condition can also be met, although the solution would not have a good fit with data.

length for a ray to provide information above the noise level is then $2.8/\sqrt{N}$ where N is the mean number of rays hitting the same voxel during a Kalman batch. We have computed an average number of 50 rays hitting each voxel for any 30 minute batch. This sets a minimum thickness of the layers in the grid of 350 m. This reasoning has been tested applying a 3.5 mm/km spike of 175 m thick first, and then of 350 m thick. As we show in Figure 5.2, the former is almost lost in the reconstructed field while the latter can be recognized.

The impact of noise has been tested. For the simulations, we have fixed the grid to 4x4x40 voxels and generated the data with the same grid to remove the discretization error. Because the system is linear, we can consider a gaussian white noise sequence as the input data. The noise power ranged from 1 mm^2 to 10^4 mm^2. For each series, the power at the output has been computed. In Figure 5.3 we show the relationship between both parameters, with two

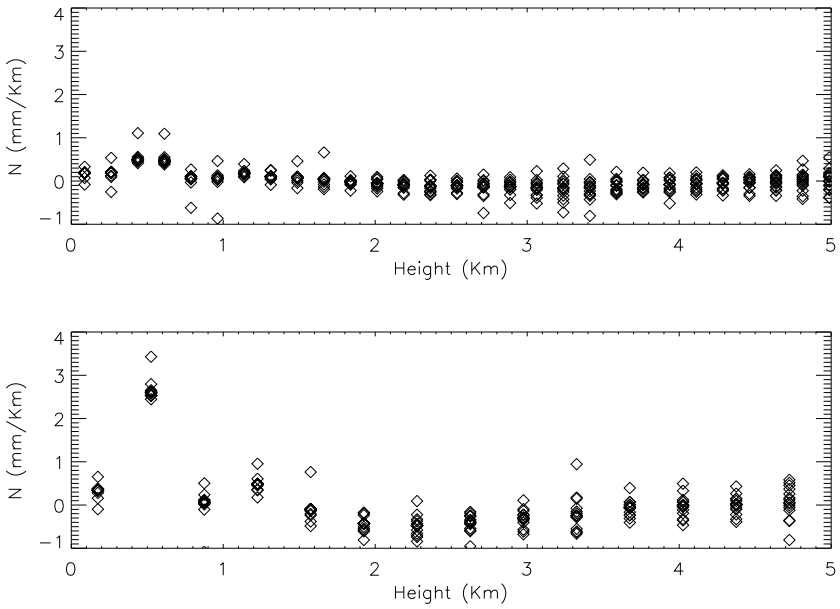

Figure 5.2: Spike analysis: response to a 3.5 mm/km spike at 350 m height with width 175 m (top) and 350 m (bottom). The noise was σ=10 mm for both.

different cut-off values. The solid solid line is for a $\nu = 2.8$ km cut-off value and the dashed line corresponds to $\nu = 1.41$ km. In the 10 mm input noise range, the linear relationship can be appreciated and as well as the corresponding 2 factor between the output noise for both cases.

For the previous analysis we have used the geometry given by the Hawaii 1997 network (see Section 5.2.2). This network has an orography that makes it particularly well suited for tomography; the vertical resolution here analyzed may be worse for other networks without such a height distribution of the stations. Regarding the impact of noise, it depends on the cut-off value for the eigenvalues, which is independent of the network. In the next section, we particularize our analysis to the Hawaii network. Results should be taken as a best-case reference.

The LOTTOS software [51] has been used to analyze simulated fields, the impact of noise and to process the real data.

5.2.2 Simulations using the Hawaii network

The Kilauea network in Hawaii is a dense local network, normally used to track ground movements due to volcanic activity ([75]). We had available a set of data used to study these movements (January 30th eruption) and for this tropospheric study we have selected a date (February 1st, 1997) when those had vanished. There are 16 stations distributed over

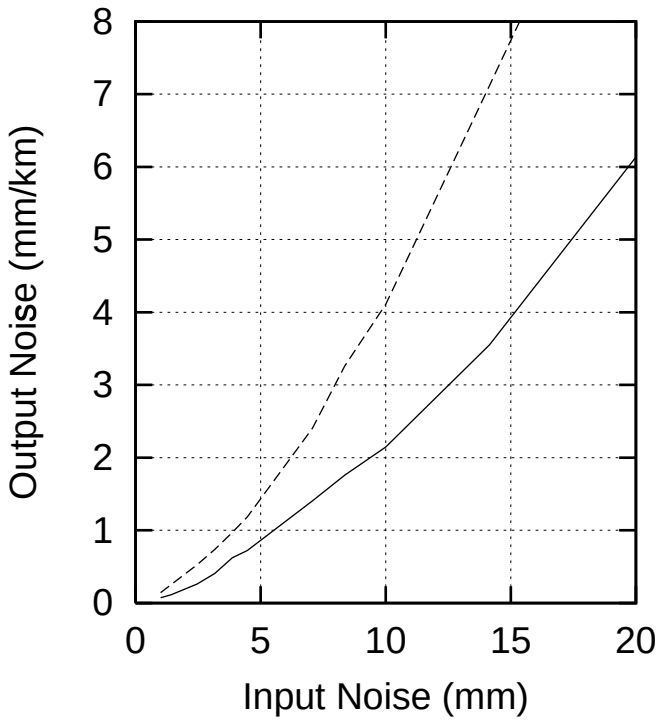

Figure 5.3: Impact of noise in the solution. Solid line is for a cut-off value of $\nu = 2.8$ km and the dashed line for $\nu = 1.41$ km.

an area of 400 km^2 (see Figure 5.4) and located at different heights that range from sea level up to about 2000 m; the elevation cut-off angle was 7^o. The height distribution of the stations is an essential factor to obtain good vertical resolution. For the simulations we have used the locations of the stations and the satellite orbits for that day (for simulations, the particular day is not a key issue, since GPS orbits are very similar from one day to another). Simulations included spike analysis, discretization error analysis and finally two cases where we took a profile from a radiosonde and from a GPS/MET occultation, applied horizontal variability and used the 3D field to simulate measurements and test the retrieving capability of the tomographic approach.

5.2.2.1 Discretization error and spike analysis

In order to determine the impact of the discretization error, we first define a regular grid of 7x7 voxels in the horizontal and 82 layers of 175 m thick up to 15 km height above the sea level to generate the delays. In horizontal, a small gradient has been applied and in vertical the radiosonde profile has been used. Additive gaussian noise has also been included. The gradient is small enough so that when a more coarse grid in horizontal is used (4x4), the discretization error is below the additive noise; we can hence analyze the impact of the layer

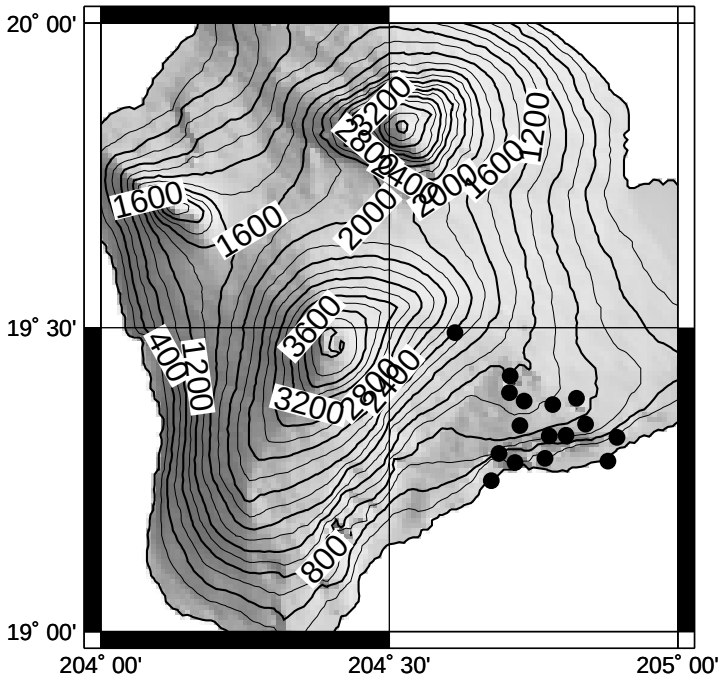

Figure 5.4: Map with the location of the stations of the Kilauea permanent network in Hawaii in February 1997.

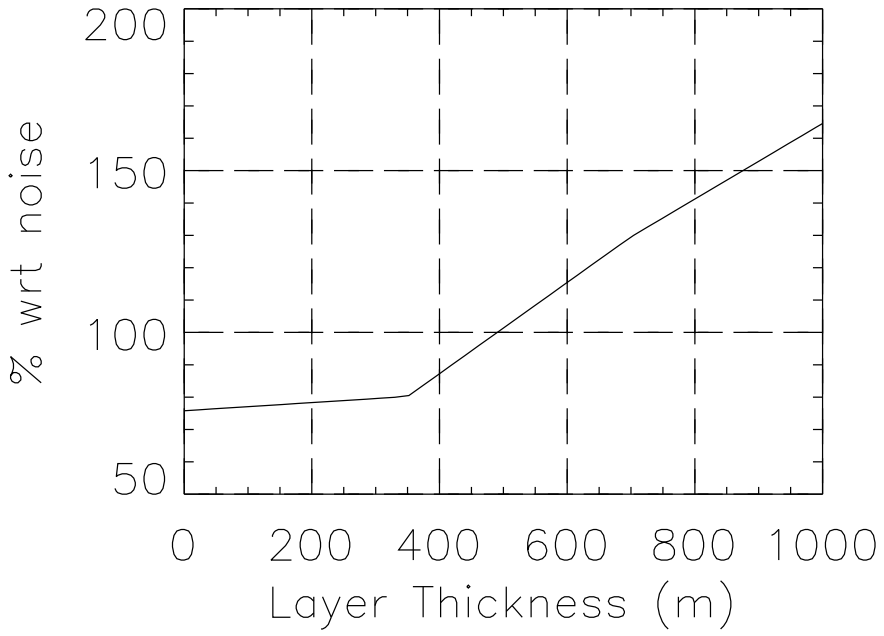

Figure 5.5: Effect of the discretization of the 3-D space: the error is shown as % of the random noise of the input data.

thickness separately from the horizontal dimension. The delays thus generated have been used as observables in a tomographic solution using 4x4 voxels in horizontal and successively thicker layers. For each run, the rms value of the residues has been computed. In Figure 5.5 we show the evolution of this value normalized to the input thermal noise (in %) as a function of the layer thickness. It is shown that the 350 m value considered is consistent with the discretization error for a typical profile.

A spike of 350 m thickness has been placed at different heights and results are presented in Figure 5.6. The parameters computed are the spread of the spike (defined as the width of the peak when it falls to 60% of the maximum value) and the relative value of the peak in the solution with respect to the original 3.5 mm/Km. It can be seen that the resolution is gradually lost as we move to higher altitudes: the peak spreads and it becomes barely noticeable. It should be noted that at the lower heights the peak is reconstructed at a 85 % of its height but that there is no spreading; this can be explained considering that, at about 600 m high, the reconstruction is almost perfect and limits the spreading of the lower height peaks. The lowering of the peak is compensated by the slightly higher value assigned to ill-determined voxels.

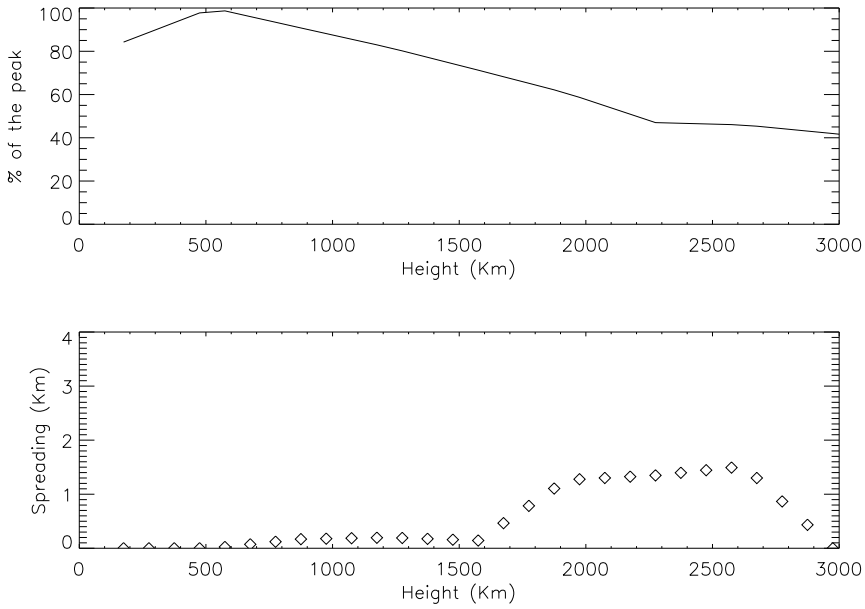

Figure 5.6: Spike analysis: response to a 3.5 mm/Km spike located at different heights. In the upper plot we show the value of the peak obtained in the solution relative to 3.5 mm/Km. In the lower plot, the evolution of the amplitude of the recovered peak to 60 % of the maximum peak value. The spreading in the lower heights is limited by the good reconstruction capabilities for data at $\approx$ 600 m.

5.2.2.2 3D refractivity field reconstruction

We have considered two 3D refractivity fields, applied them to compute the simulated delays and then we have added a gaussian white noise (σ_n = 10 mm) to each ray. Thus, we do not consider here the discretization error. We want to test the capability of the tomographic solution to reproduce a given field.

In a first simulation we have applied a refractivity field based on the vertical profile given by a radiosonde measurement obtained from a launch at Madrid, December 1, 1998, and superimposed a horizontal linear gradient. We have defined a 4x4x40 voxels grid over the area. The amount of data spanned for 30 minutes, to simulate the Kalman filter batches. The weights of the three sets of constraints are tuned so that no eigenvalue is below the cut-off threshold of 8.1 km^2. With this implementation, the tomographic inversion has provided the results shown in Figure 5.7. The reconstruction follows the original field well within the 3.5 mm/km error upper bound. The histogram of errors shows a high spike around the zero value corresponding to the higher layers of the field. The mixing ratio profile measured by the radiosonde and the GPS tomography are in very good agreement: both show a very well mixed boundary layer below 1000 m. The mixing ratio peaks at 1800 m, showing a greater amount

of water vapor below the temperature inversion. At altitudes above 3000 m the tomographic solution is smoother than the profile measured by the radiosonde, showing that (as predicted by Figure 5.6) tomography looses resolution at 3-4 km height; however, it still can follow the quasi-linear decay of mixing ratio in the free troposphere.

As a second example, we have used the vertical profile given by a GPS/MET data processed for occultation at 49.2S, 303.2E (northeast of the Falkland Islands) on June 23, 1995 at 04:07 UT (the profile was provided by E.R. Kursinksi, and appears in [20], pg 7-21; details on the occultation mission and data processing can be found in [76] and [63]). These data were selected because of the irregular vertical structure: the profile shows a rapid decay of mixing ratio in the first 2 km and a relative maximum in mixing ratio near 600 mbar; this is probably due to an occluded front, according to [20]. It is particularly interesting for our testing purposes because it requires good vertical resolution up to 6 km, higher than in the radiosonde profile. Regarding the horizontal variability, we applied a gaussian distribution almost centered over the network. Following Figure 5.6, at 3-4 km the resolution is poor, but we have surmounted this loss by considering a longer batch of data (60 minutes) and thus providing more sensing rays to the system, reducing the indetermination. Using this 1-hour batch, we obtained the results presented in Figure 5.8. Focusing on the mixing ratio profile comparison, again we observe a very good agreement, even when sensing the occluded front at 4 km. This reveals a trade off between spatial and temporal resolution. When implementing a Kalman filter, the increased resolution provided by the temporal smoothing will depend on how loose we leave the filter.

5.2.3 Tomography using a flat network

The Kilauea network in Hawaii has peculiar characteristics that make it well suited for tomographic purposes: the stations are well distributed in height and range from sea level up to 2 Km within 20 Km in horizontal. This eases the discrimination between layers. However, in most of the occasions, local orography does not allow such a height distribution of receiving stations.

Let us consider a flat network sensing a flat, layered atmosphere, with no horizontal variation. In such geometry, given a solution compatible with the data, one can form another solution by simply interchanging two layers: therefore there is no possible vertical resolution.

Nevertheless, this is not the case in tropospheric tomography: the atmosphere is not considered to be flat and it usually has some horizontal variation.

The grid considered in the tomographic solution is always spherical and spans over the minimum angle needed to include the lowest elevation observations (7^o generally) scanning

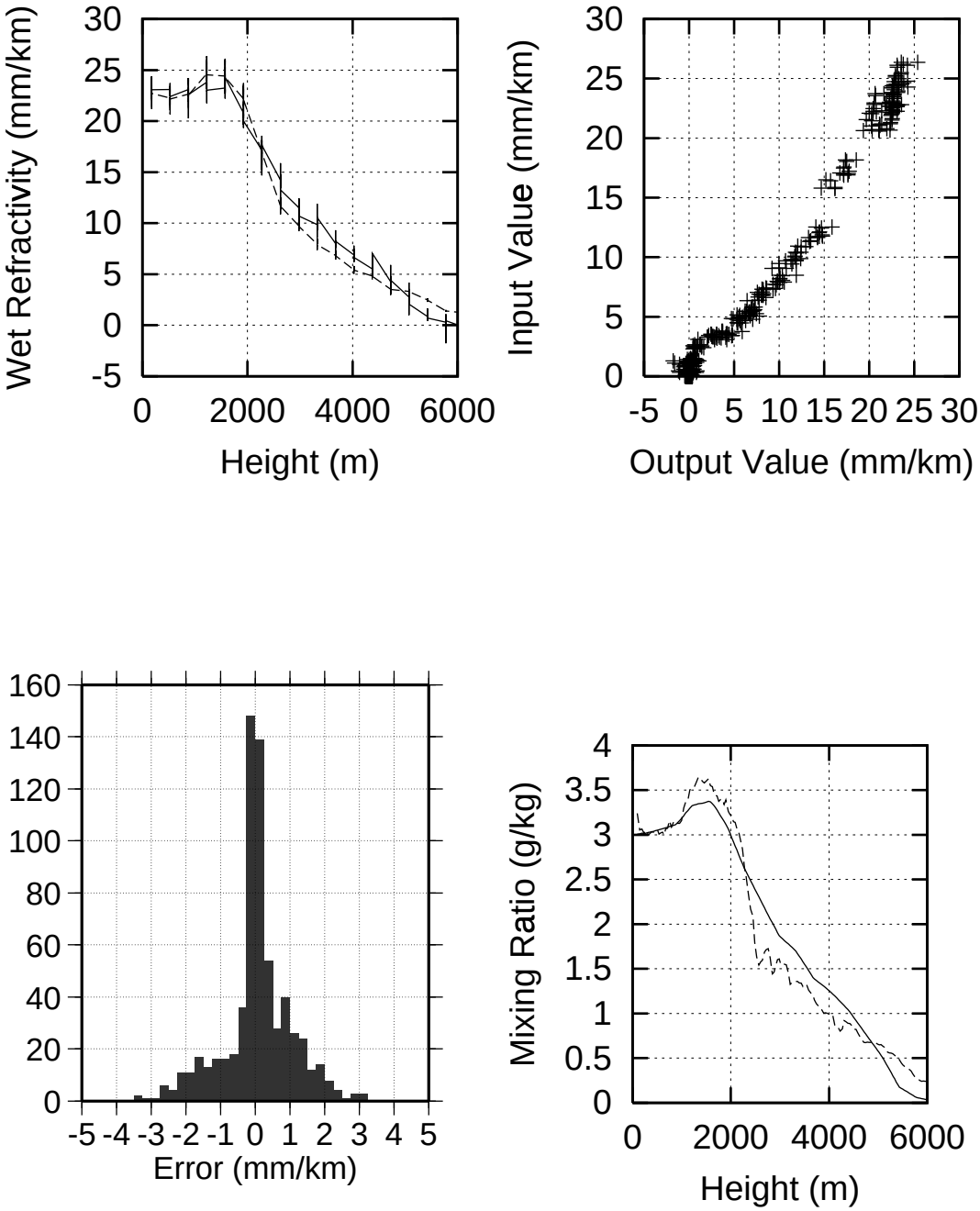

Figure 5.7: Results of the simulation using a radiosonde profile: top left, the two fields as a function of height (solid line is the reconstructed field and dashed line the original field); top right, input vs. output values; bottom, histogram of errors and vertical profile (solid) compared with the one given by the radiosonde used for the generation of the field (dashed).

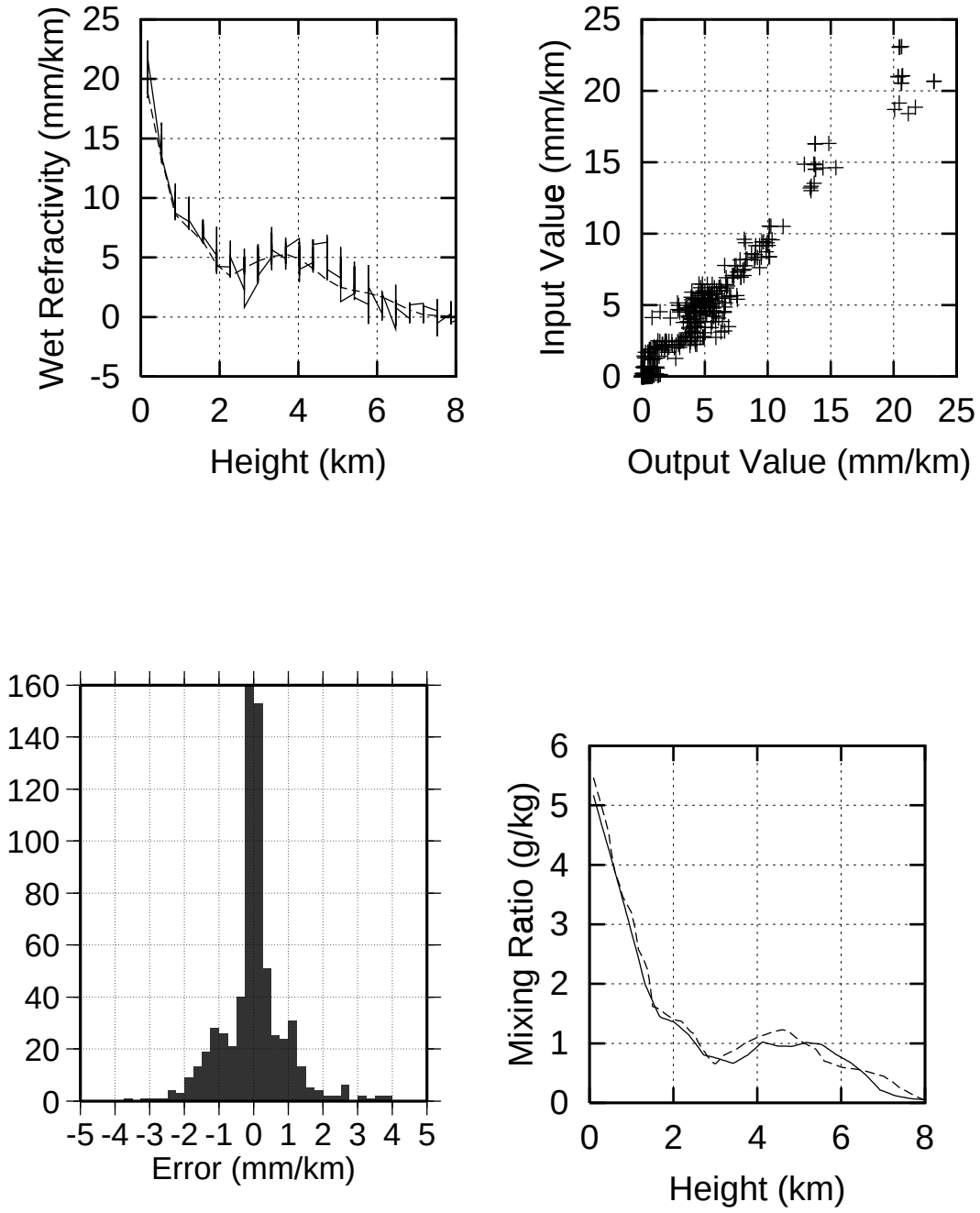

Figure 5.8: Results of the simulation using a GPS/MET occultation and a 60 minute batch: top left, the two fields as a function of height (solid line is the reconstructed field and dashed line the original field); top right, input vs. output values; bottom, histogram of errors and vertical profile (solid) compared with the one given by the GPS/MET occultation data used for the generation of the field (dashed).

the atmosphere from the surface up to 15 km height. This leads to an arc-length of 2^o in each direction to define the grid. Simulations in Section 5.2.3.2 have shown that even when reducing the arc-length to 1^o, the tomographic reconstruction has some vertical resolution.

Regarding horizontal variation of the atmospheric field, it does not play any role in the singularity of the linear system, since the singular values of $\mathbf{S}$ do not depend on the data. However, certain features in the observed field comply better with the apriori knowledge and the solution can provide a better fit. Let us consider the probabilistic view presented in Section 3.3: when the data are such that the associated model parameters comply with the apriori knowledge, the solution will have a more distinctive maximum likelihood point and the residues will be smaller. In such a case, the different possible solutions are more likely to lie within the expected output variance. We can therefore analyze the capability of the system to locate gradients.

5.2.3.1 Gradient Impact

In order to prove the capability of locating gradients at different heights using a flat network, we have considered 25 stations evenly distributed forming a 5x5 km square, and the GPS constellation during 1 hour. The refractivity field has been defined as a spike at different heights, with a superimposed linear gradient in the North-East direction. The spike was centered at 250 m, 750 m, 1250 m and 2500 m height.

We show in Figure 5.9 the magnitudes of the north and east components, simulated and reconstructed. In all cases, the gradient is spread to the neighbouring layers, but it is clearly visible, particularly at 750 m and 1250 m heights. At low heights and 2500 m, the spread is larger, as well as the error in magnitude. We can therefore be confident that our results within the initial 1-2 km of the troposphere will reflect the actual water vapor structure. To further prove this, we have conducted, as in the Hawaii case, two simulations using measured humidity profiles, as we discuss in the next section.

5.2.3.2 3D refractivity field reconstruction

Considering the 25 stations flat network, we have constructed a 3D refractivity field, considering the Madrid radiosonde profile and superimposing a linear gradient in the North-East direction. The grid consisted of 4x4 voxels every layer and layers are 400 m thick. In order to define the horizontal extension of the grid, we have considered two minimum elevation angles, 15^o and $7\ ^o$, which define minimum arc-lengths of 1^o and 2^o respectively, being the solution using the latter slightly better. We present the results in Figure 5.10. The weight on the boundary condition is rather small, and therefore, most of the vertical resolution is

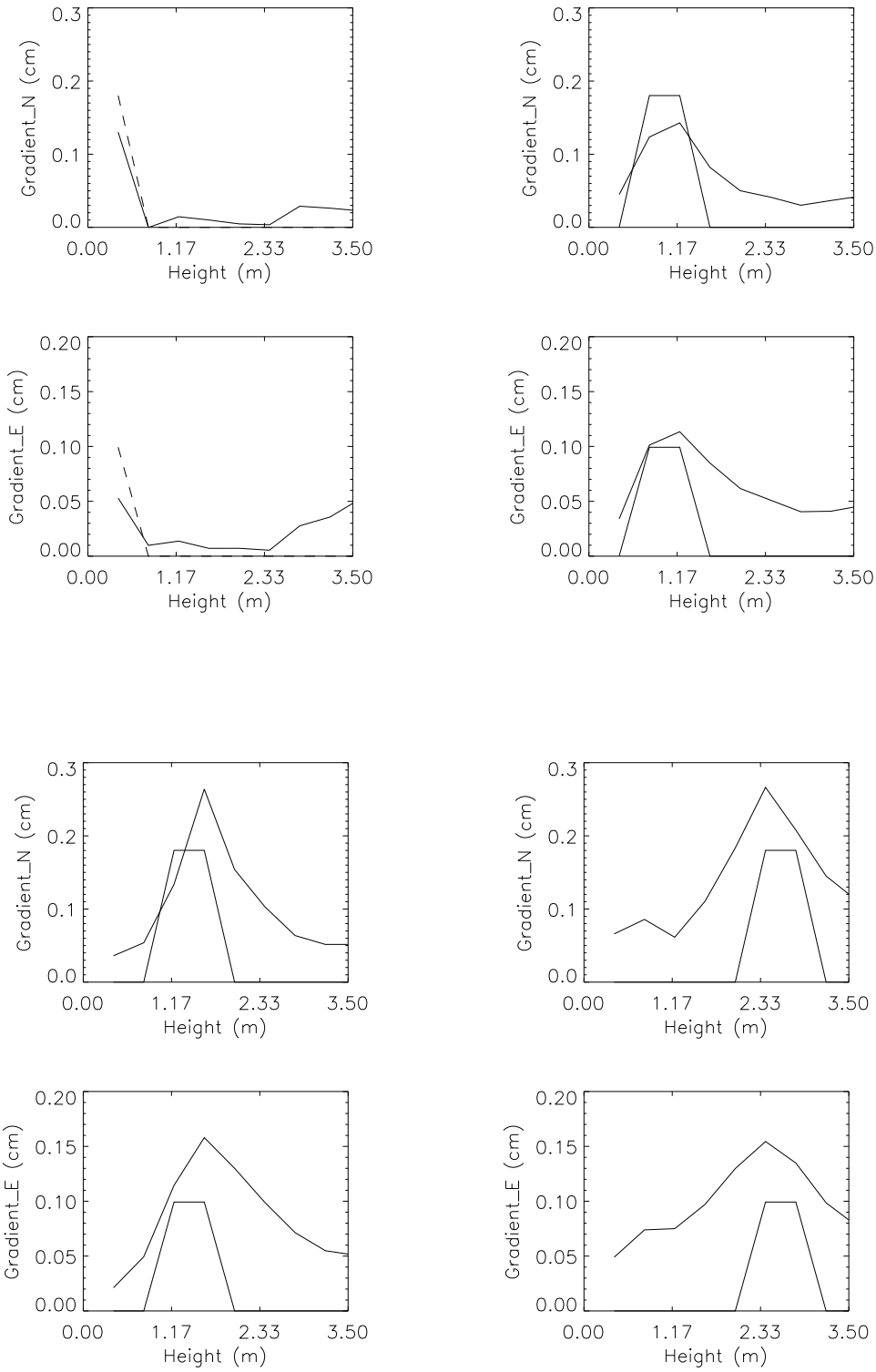

Figure 5.9: Results of the simulation with the 25-stations network placing a spike with a gradient at different heights: from top to bottom and left to right, centered at 250 m, 750 m, 1250 m and 2500 m. In the 250 m the original spike is drawn in dashed line. It can be seen that there is a good reconstruction of the linear gradient from 750 m and higher.

given by the observations. The tomographic solution still captures the well-mixed layer below 1000 m, though the 1800 m maximum is smoothed and slightly displaced to 1500 m. The vertical profile above 2 km is much smoother in the tomographic solution than the radiosonde measurement. The level of agreement is not as good as when using the Hawaii network. However, there is some vertical resolution with ground tomography, even with a flat network, and we thus confirm that a curvature of the grid of even 1^o is sufficient for a 25 km^2 network is enough.

As a second example, we have applied the profile derived from the GPS/MET occultation, superimposing a gaussian horizontal variation. In this case, and as we saw in the gradients simulations, resolution at 4 km is expected to be poor, even when using three hours of data. Results are presented in Figure 5.11. The occluded front at 4 km does not appear in the solution and the sharp decay in the first 1000 m is slower in the tomographic solution. In the Input value vs. output value plot, the points are not aligned anymore, a clear indication that the solution is averaging the values at different heights to yield a minimum quadratic error, though incorrectly reproducing the input field.

This important difference between the solutions obtained using the Kilauea network and the 25-stations network clearly highlights the key role of the network geometry. Obviously, having stations at different heights greatly enhances the vertical resolution. However, this capability is dictated by the local orography and little can be done to overcome it, apart from using receivers on board airplanes or balloons or occultation data. Regarding a ground network, nevertheless, the location of the receivers does determine the resolution, as shown in the next section.

5.2.3.3 Network geometry considerations: a link with antenna theory

In this section we follow a heuristic reasoning to establish an analogy with antenna array theory. Assumptions made may be too simplistic but we just pretend to provide qualitative representations.

Let us assume a flat network and a simple 2D model to understand where the best resolution appears. In order to do that, we consider a case with two stations (A and B) viewing two satellites (C and D). Then, the two links AC and BD will intersect forming an angle α. The geometrical locus of all the points with the same value of α is a segment of circumference that includes points A and B. When $\alpha = \pi/2$ the point is perfectly determined since rays are orthogonal (if rays are parallel, they provide no further information than just one of them). Thus, the locus of points that will be perfectly determined by these two pairs of stations and satellites is the circumference that has AB as diameter. The highest point will be located

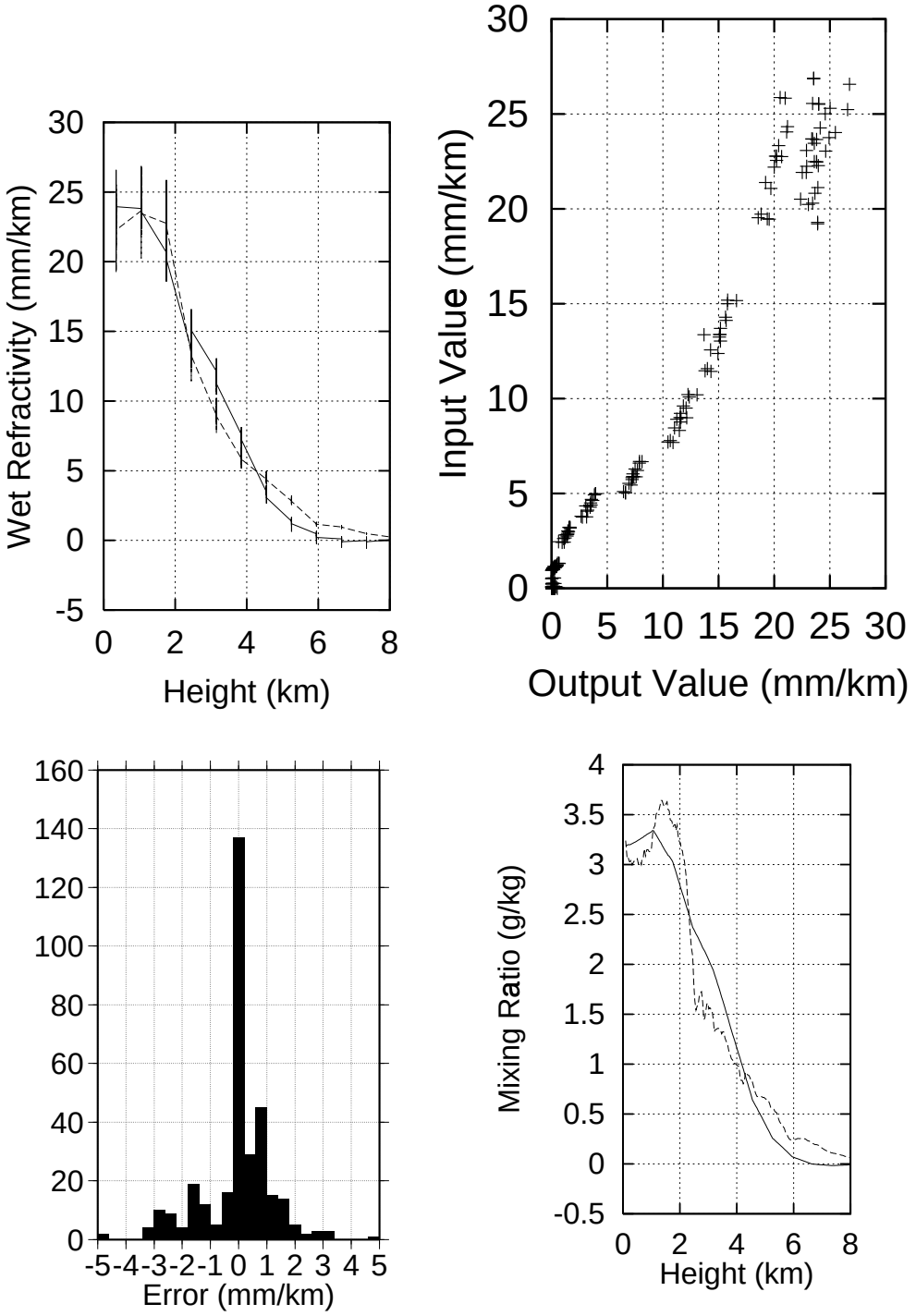

Figure 5.10: Results of the simulation with the 25-stations network using a radiosonde profile: top left, the two fields as a function of height (solid line is the reconstructed field and dashed line the original field); top right, input vs. output values; bottom, histogram of errors and vertical profile (solid) compared with the one used for the generation of the field (dashed).

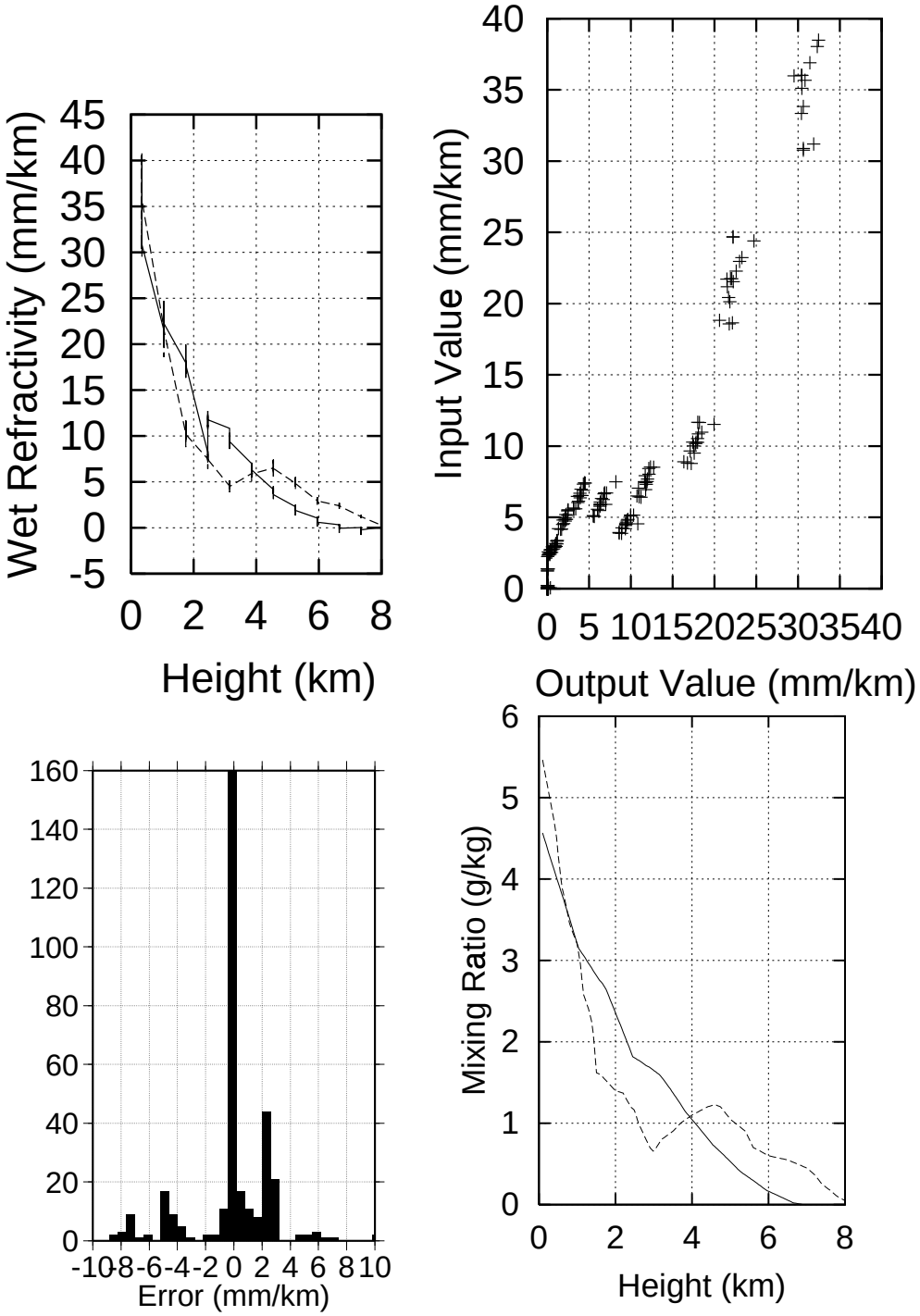

Figure 5.11: Results of the simulation with the 25-stations network using a GPS/MET occultation: top left, the two fields as a function of height (solid line is the reconstructed field and dashed line the original field); top right, input vs. output values; bottom, histogram of errors and vertical profile (solid) compared with the one given by the radiosonde used for the generation of the field (dashed). It is clearly seen that the vertical resolution at 4 km high is lost.

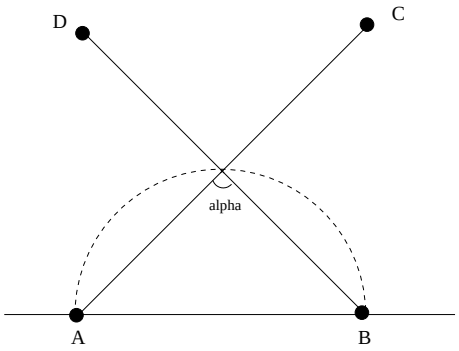

Figure 5.12: Simplified model of the inverse problem in tomography.

over the midpoint of AB and at a height equal to $d/2$ where d is the base-length (see Figure 5.12). We therefore see that there is a dependency on the base-length of the vertical location of good resolution. This has parallelism with the antenna array theory, in which the distance between elements determines the radiation diagram. There are, however, differences in both cases that may occlude the translation from one field to the other: the array factor is derived considering that the source is far away and *common* to both receivers and it is a consequence of destructive and non-destructive interference. In tomography, we are considering *different* sources.

Nevertheless, the link with antenna theory can be used to develop some intuitive and qualitative characterization of a tomographic network.

An array of antenna elements has specific properties such as directivity that depend on the *electrical wavelength* distance between elements, and hence, there is a frequency dependency of such parameters. In the case of tomography, there is a dependency of the location of well determined points on the *spatial base-length* between receivers. Importing some concepts from antenna theory, we can therefore obtain a better understanding on the best suited configuration of receivers of a ground network to yield the best tomographic solutions. The most immediate application is the obtainment of good resolution at as many heights as possible, with the minimum number of receivers. This is an analogous problem as to obtain *broadband antennas*. In [77] it was demonstrated that if an antenna has a geometry that can be described only as a function of angles, it will be frequency independent since a scaling factor will not change it. Furthermore, an antenna will be auto-scalable in the case that the geometry doesn't change when it is multiplied by a scale factor k. In such a case, it will present the same characteristics at frequencies f and f/k. Similar concepts can be applied to tomographic networks. We have seen that the well-resolved voxels lie at a height of $d/2$. If we want to determine voxels at $(k \cdot d)/2$ we need a base-length of $k \cdot d$. Hence, we need to find this base-length in the array just by rotating the network around its axis. The array should then

be *auto-scalable*.

A very common geometry in broadband antennas is the spiral. It can be expressed as:

$$r(\theta) = Ae^{a\theta} \tag{5.6}$$

and, if we scale the geometry [78]:

$$kr(\theta) = kAe^{a\theta} = Ae^{a(\theta+\frac{1}{a}\ln(k))} = r(\theta + \Delta\theta) \tag{5.7}$$

Therefore, in tomographic studies, one should use the spiral distribution of receivers. That was almost the case of the local network of the Onsala experiment, REGINA, which we will analyze in a later section.

At this point, we leave the further insight in the correspondence between antenna theory and tomographic networks for a future work, but highlighting that it can be, in fact, a useful tool in designing tomographic networks.

5.3 Results with experimental data

5.3.1 Results from the Hawaii network on Feb. 1, 1997

5.3.1.1 The Network and the Tomographic Processing

We have processed data from 16 stations in the permanent Kilauea network for February 1st, 1997. We have used a grid of 4x4 voxels (6' in latitude and 7' in longitude) (see Figure 5.13 [§]), 40 layers of 350 m thick and 30-minute batches for the Kalman filter. The GPS data have been processed using GOA II. The time series of zenith wet delay, gradients and residuals have been combined into the SWD. In order to calibrate the weights of the constraints we have followed the same procedure as in the simulations. The Kalman filter is run forward and backwards with a uniform $\delta = 2$ (mm/km)$/\sqrt{h}$.

The residues of the tomographic fields (σ =6.1 mm) and of the GOA II processing (σ=7.6 mm) are shown in histograms in Figure 5.14; in Figure 5.15 their dependence with elevation, together with the GOA II processing residuals. Both histograms are similar with the tomographic fit having a lower σ value, thus indicating that tomography provides a better fit in the determination of the 4D distribution of wet refractivity: the zenith and gradient time-series at each station are, in fact, an average value of the refractivity in the vertical dimension, while tomography permits a correct location of different features in height, therefore representing the same field with more parameters, providing more information. However, the tomographic

[§]Maps are labeled in degrees; a rule-of-thumb to convert to distance is that 1^o corresponds to 100 km close to the equator.

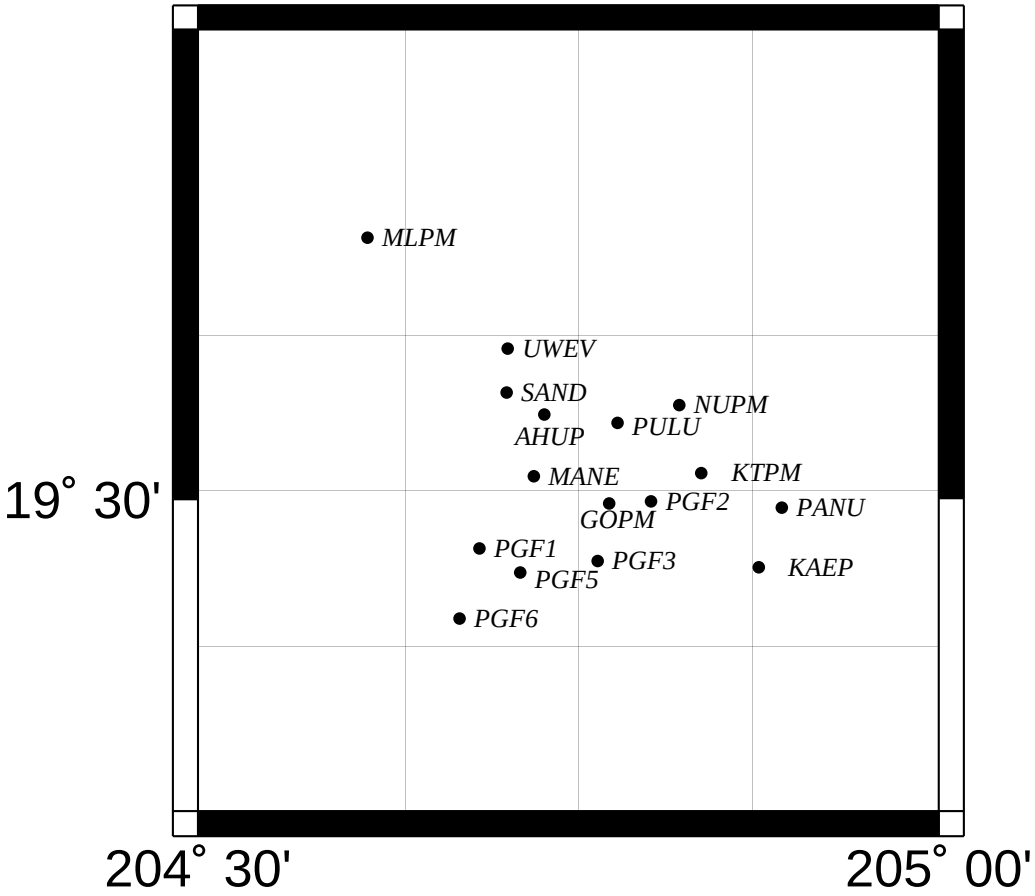

Figure 5.13: Grid used in the Hawaii 1997 experiment. Note that each voxel is about 10 km x10 km.

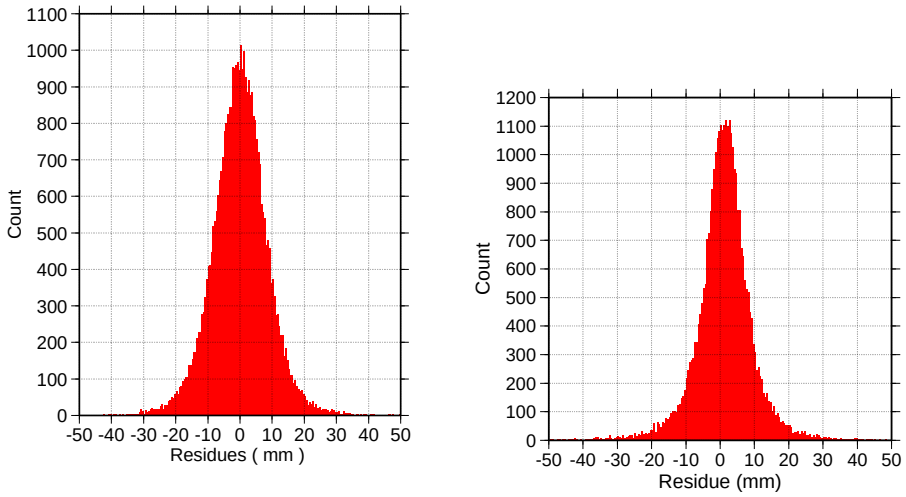

Figure 5.14: Histogram of the residues of the GOA II processing (σ = 7.6 mm) (left) and tomographic solution (σ = 6.1 mm) (right) for the Hawaii data.

residues have a stronger dependence with elevation than GOA II processing: this is because the Niell mapping function considers correcting terms that account for the ray bending in a standard atmosphere, while our tomographic approach considers, for the sake of simplicity, no bending of the observables due to the refractivity field (otherwise, the inverse problem would not be written in an explicit form); in a future refinement of the technique, the ray bending should be considered. In fact, the full ingestion of GPS slant delays into a numerical weather prediction model with full consideration of ray bending would be the ultimate goal for a 4D representation of the troposphere. Notwithstanding, tomography still provides an accurate representation of the spatio-temporal structure of the refractivity.

5.3.1.2 Interpreting the tomographic solution

In order to further prove that the obtained fields are compatible with the observables, we have reconstructed the SWD from the tomographic fields and then calculated the time series of the horizontal delay gradients and ZWD for each station. These have been compared to those obtained with GOA II from the original data. The time series of the ZWD and the two components of the delay gradient are presented in Figure 5.16 for a particular station (PGF3) and in Table 5.1 the correlation values over time for each station. This, however, just proves the consistency between solution and data over the time span.

The vertical refractivity field is shown in Plate 1 for latitudes 19^{o}16' and 19^{o}37' and for times between 07:30-08:00 UT. The orography is also represented.

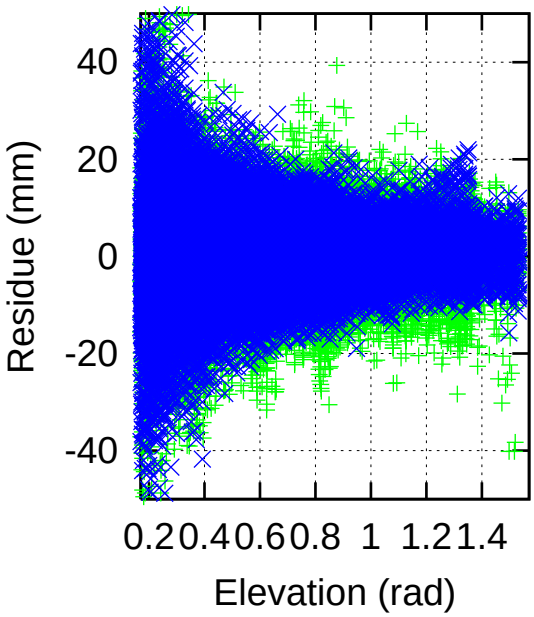

Figure 5.15: Dependency of the residues of the GOA II processing (green) and Tomography (blue) with respect to elevation. The tomographic solution shows a better scatter of residuals though roughly the same elevation dependence. This is due to good agreement of the mapping function with the structure of the atmosphere for this particular case.

Station	ZWD	North	East
AHUP	0.98	0.80	0.83
GOPM	0.96	0.79	0.64
KAEP	0.98	0.78	0.71
KTPM	0.97	0.57	0.72
MANE	0.98	0.90	0.70
MLPM	0.99	0.55	0.88
NUPM	0.97	0.62	0.53
PANU	0.99	0.53	0.43
PGF1	0.98	0.83	0.83
PGF2	0.97	0.74	0.78
PGF3	0.97	0.86	0.86
PGF5	0.97	0.85	0.84
PGF6	0.97	0.88	0.89
PULU	0.98	0.56	0.41
SAND	0.99	0.61	0.82
UWEV	0.99	0.69	0.82

Table 5.1: 24-h correlation factors for the ZWD and the Total Horizontal Gradients in both components, North and East, for each station.

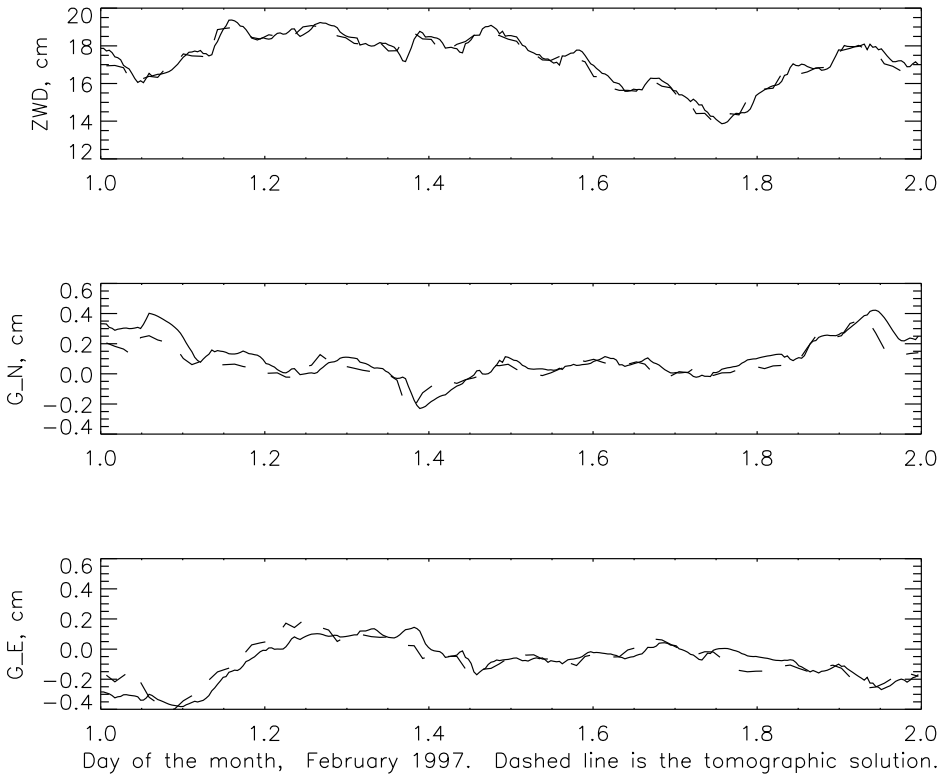

Figure 5.16: Comparison of the time series of the GOA II solution and the tomographic solution (dashed) for the Zenith Wet Delay (ZWD) and the North and East components of the gradients (G_N, G_E). The good matching ensures a good fit in time of the tomographic field to the input data.

5.3.1.3 Verification of the results: comparison with ECMWF analysis

In order to verify this structure, we have computed the values of $N_w(\vec{r}, t)$ profiles from the European Center for Medium-Range Weather Forecast (ECMWF) ([79]) analysis and compared them with our tomographic profiles taking a mean value of all the voxels in the same layer to meet the ECMWF maps resolution of 0.5 degrees. Results are presented in Figure 5.17 for the three different time stamps (06h, 12h, and 18h) for which we have the ECMWF maps, showing good agreement. It can also be seen that ECMWF forecasts predict a smoother time variation than tomography shows, which is expected given the unpredictable behaviour of the water vapor contents in the troposphere. The differences between ECMWF forecasts and tomography cannot be taken as an indicator of the tomographic field being close to other measurements with the accuracy estimated in previous sections, given the great differences in resolution between the two analysis. However, the agreement in vertical scales and in orders of magnitude of the solutions does provide evidence that the tomographic solution correctly represents the wet refractivity spatio-temporal evolution. The final comparison should contemplate on-site measurements as given by radiosondes. Unfortunately, the closest radiosonde launch site is at Hilo, where troposphere is most of the times uncorrelated with the observed over the Kilauea permanent network (Mike Bevis, private communication). Thus, no comparison with radiosonde data was done due to the unavailability of such data in the area considered for the day processed.

5.3.1.4 Conclusions from the Hawaii 1997 data

The previous comparison and the good results obtained with simulated data allow to conclude that tropospheric tomography is feasible and particularly with networks that present a mountainous orography: the GPS receivers are naturally placed at different heights, thus enhancing the vertical resolution. This network is useful to obtain initial results before exploring the capabilities of flat distributions of receivers. The results concerning the Hawaii network were published in [80].

5.3.2 Results from the REGINA Campaign at the OSO

5.3.2.1 The Network and the Tomographic Processing

During three weeks in August, 1998, six GPS receivers were deployed close to the IGS site in Onsala. The experiment was mainly conducted by Lubomir P. Gradinarsky and Pedro Elósegui, with the support of the Onsala Space Observatory (OSO) and the Center for Astrophysics at the Harvard-Smithsonian Institute (CfA). The so-called REGINA experiment

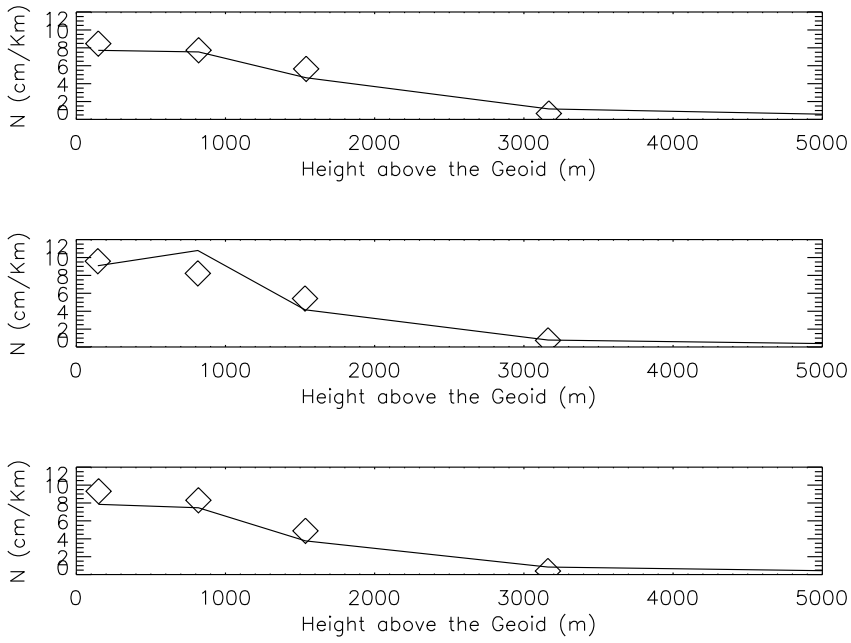

Figure 5.17: Comparison of the tomographic profiles with the ECMWF analysis for the same area at epochs 06h, 12h and 18h. ECMWF analysis have a poorer time and space resolution.

([40], [81]) included, as well, two water vapor radiometers. The purpose of REGINA was to obtain a continuous set of data for local atmospheric studies. The location of the receivers is shown in Figure 5.18.

Although the experiment was designed without considering an optimal network for tomography, and the sites were decided upon base-lengths and accessibility considerations, it turned out that the geometry of the receivers followed to some degree the spiral distribution that was discussed in Section 5.2.3.3 as a broadband configuration. It was, therefore, a great coincidence to be exploited in order to explore the capabilities of tomography.

The GPS data were analyzed using Bernese and GIPSY-OASIS II at OSO and at CfA. The data series showed one particular day, 24th August 1998, in which strong gradients were detected. The results published in [40] compared the two types of gradients $\vec{L}^G$ and $\vec{G}$, and revealed the existence of a lag between the time series of $\vec{L}^G$ and $\vec{G}$, which was there explained as a refractivity gradient field entering from the north with the "leading edge" occurring at a higher altitude than the "trailing edge". Such qualitative explanation was later corroborated with the tomographic solution.

We reprocessed the August 24, 1998 data using the GOA II software and the LOTTOS/GIST software package. The ZHD was extracted from pressure measurements at the

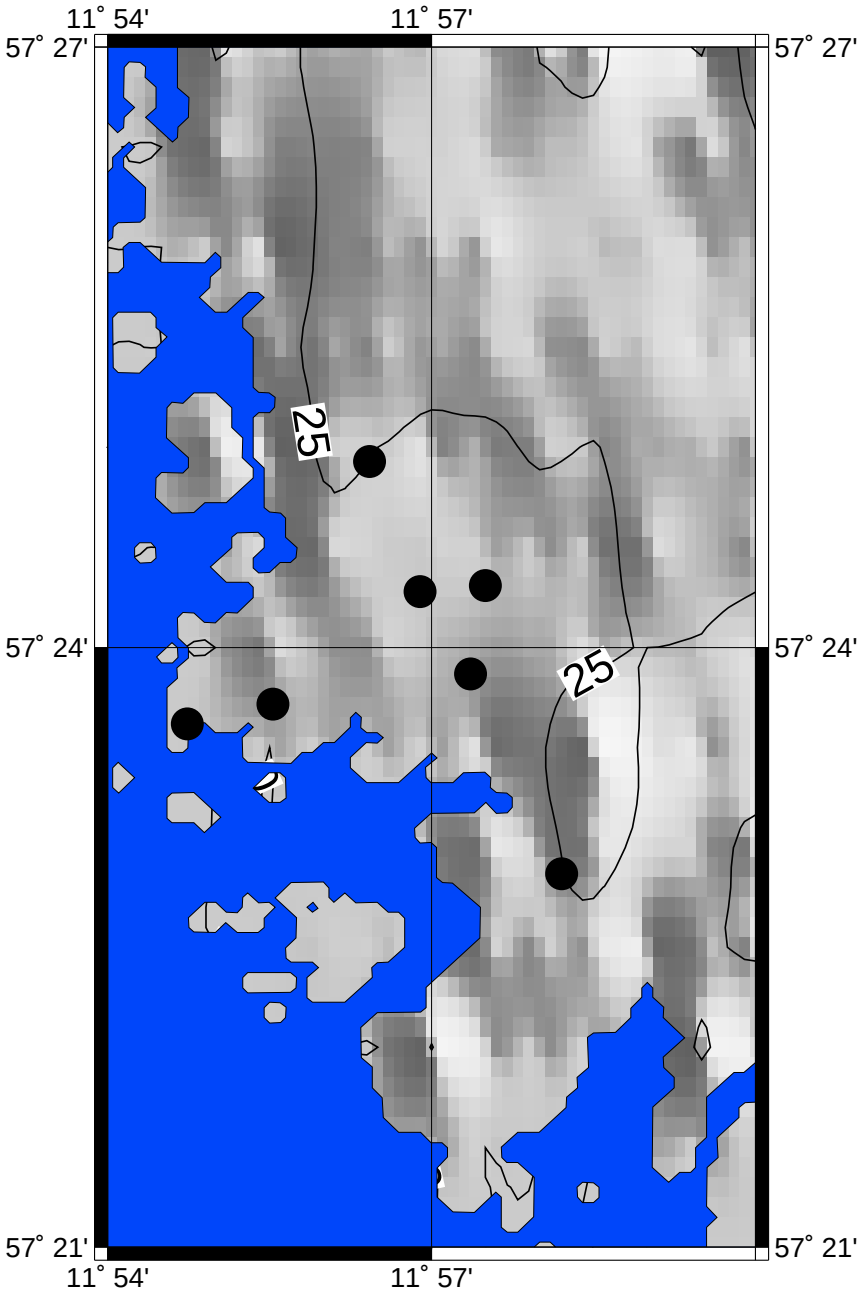

Figure 5.18: Map with the location of the stations of the REGINA campaign at the Onsala Space Observatory during the summer of 1998. Curves of height above the geoid are also plotted (elevation data from the USGS archive, http:/edcwww.cr.usgs.gov/landdaac/gtopo30/gtopo30.html).

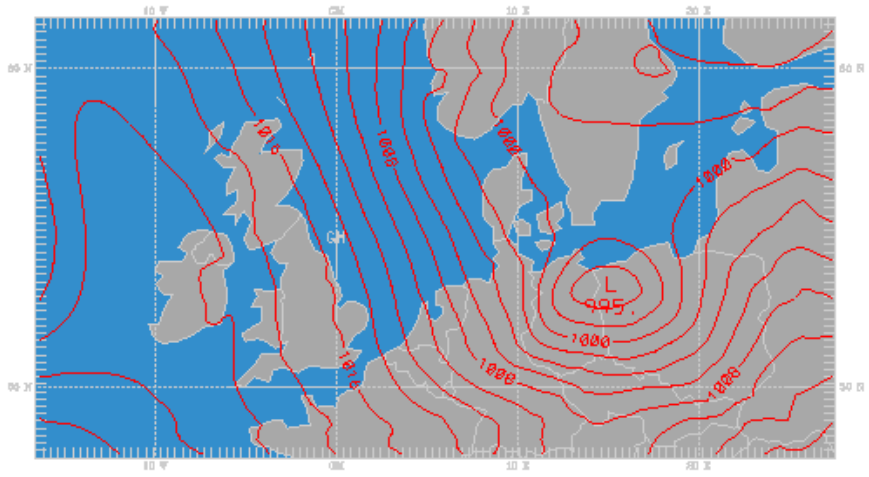

Figure 5.19: Surface pressure map at 12:00 UTC from MM5 analysis. The Onsala IGS site is at 11.925^o E, 57.22^o N.

IGS site and hydrostatic gradients were considered negligible, judging from the MM5 analysis that shows the Onsala peninsula free from surface pressure gradients during the first 21 hours of the day (see the situation at 12:00 UTC in Figure 5.19).

The tomographic solution considered a grid of 6x6 voxels at each layer height (as shown in Figure 5.20), 26 layers of 400 m thick and 96 batches of 900 s each. The Kalman filter was run forward and backward with a uniform $\delta = 2$ (mm/km)/$\sqrt{h}$. We have plotted the solutions for different batches in 3D, plotting some isosurfaces to clearly visualize the leading edge of the refractivity gradient.

5.3.2.2 Interpreting the tomographic solution

In a first analysis, it is interesting to trace the similarities between the tomographic analysis and the results published in [40] and here reproduced in Figure 5.21. There is an initial increment of the north component of $\vec{L}^G$ at around 6:00h UTC, but nothing is detected in $\vec{G}$. This is due to the different weight given to the gradients at different heights. In Plate 2 a refractivity gradient is entering from the north-west, with a leading edge at around 800 m, at latitudes close to 57.7^o (note also that in Figure 5.21 the east component of $\vec{L}^G$ is slightly negative). At UTC 09:15 a north gradient is strong at 1200 m and starts to appear at surface level, the east component of the gradient at higher altitudes is important within the north-east corner (Plate 3). Note that in Figure 5.21 the north component of $\vec{G}$ starts to increase, while $\vec{L}^G_N$ peaks, and there is a noticeable positive value of $\vec{L}^G_E$. At 12:15 UTC, the gradient at low altitudes is mostly towards the north around the IGS site and again strong

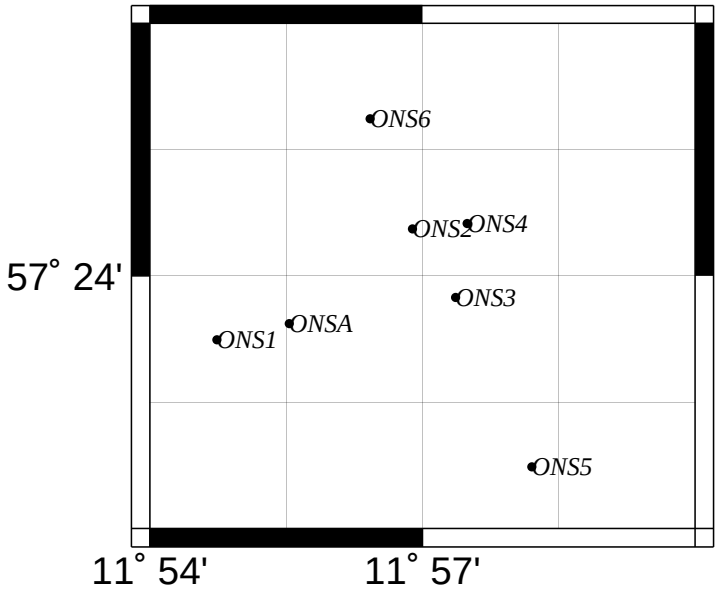

Figure 5.20: Grid used in the REGINA experiment. Each division in latitude is 0.0125^o and in longitude is 0.025^o.

at 57.7^o north at 1200 m (Plate 4), where a relative maximum of mixing ratio is detected at 1200 m. This will become more clear in the soundings obtained through the tomographic solution. Finally, the high wetter layer vanishes in the afternoon and at around 18:00 UTC it is no longer present. At that time, a small gradient is crossing from the south, as seen in the tomographic reconstruction.

It is worth mentioning that, while the tomographic reconstruction gives a richer description of the troposphere, in terms of space and time (particularly in terms of vertical distribution), the results are obviously driven by the zenith plus gradients solution of the GPS data processing: we have seen that even small gradients are reproduced by the 4D solution. Therefore, it is a key aspect to remove the hydrostatic gradients prior to any further processing, in order to correctly interpret the results. For the REGINA campaign we were limited to numerical weather models to compute the hydrostatic gradients (which were seen to be negligible), but in further campaigns on-site measurements should be included to compute $\vec{L}_h^G$.

The above discussion proves that tomography provides a good spatio-temporal representation of the troposphere, consistent with a finer interpretation of the gradient analysis, and is able to better observe and quantify atmospheric phenomena which can be relevant in meteorological studies, such as the formation of a layer close to saturation above the atmospheric boundary layer (see the meteorological analysis of Section 5.3.2.3).

In the following sections we provide evidence of the agreement of results with those obtained using more traditional meteorological tools such as radiosondes and numerical models.

5.3.2.3 Verification of the results: Discussion of the meteorological situation over Onsala on the 24th August 1998

Information was gathered from the weather charts from the Deutscher Wetterdienst (DWD), the NOAA satellites pictures (AVHRR data) in channels 2, visible, and 4, infrared, as well as radiosonde data from launches at Goteborg-Landvetter airport (57.67^{o}N, 12.30^{o}E, about 40 Km from the REGINA experiment) and simulations using the numerical weather prediction model MM5[¶]. The intercomparison of the above mentioned methods to GPS tomography was in good agreement, showing the maximum of wet refractivity in a layer above the surface layer; consequently, it provided the final evidence that tropospheric tomography is feasible and yields correct values of the water vapor fields.

The DWD charts for 00:00 UTC show two low pressure fields located north of the Scandinavian Peninsula (minimum pressure of 986 hPa), and west of Denmark, over the North sea

[¶]Simulations in the numerical model context refers to the meteorological conditions predicted by the model for a certain region after initialization of the model with experimental data

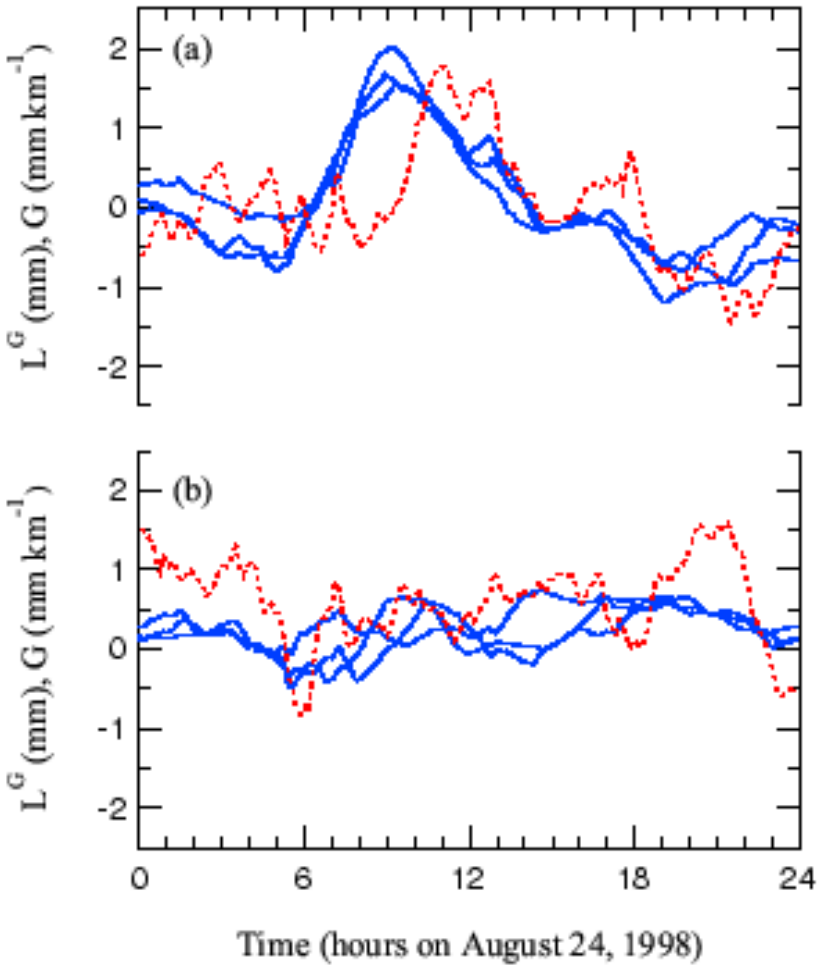

Figure 5.21: Delay gradients for three stations during 24th of August 1998 for the north (top) and east (bottom) components (blue solid). There is a clear gradient to the north, which is two hours ahead from the corresponding $\vec{G}$ value (red dashed) (from [40]).

(minimum pressure of 996 hPa). At 12:00 UTC the second low pressure field moves easterly (now north of Germany) and there are low winds on the surface. This synoptic-scale analysis shows that the GPS network area is not directly influenced at 10-12 UTC by any of these fronts.

Radiosonde data at Goteborg-Landvetter airport represent the closest measurements of temperature, moisture and wind velocity and direction profiles to the Onsala site. In Figures 5.22 and 5.23 we show the skew-T diagrams given every 6 hours for 24th of August (see Appendix B for details on what skew-T diagrams represent and the relation of temperature T and dew point T_d with mixing ratio). The radiosonde data may be interpreted as follows:

At 00:00 UTC, due to longwave radiative cooling at the Earth's surface, there is a small temperature inversion and $T = T_d$[‖], leading to the formation of a moist layer, which can be associated with fog formation. At 06:00 UTC, this moist layer moves slightly up to 925 hPa, and wind (with NE direction) is relatively low near the surface. At 12:00 UTC, the sounding confirms the existence of a layer at 825-800 hPa which is closer to saturation than the surface layer. Also, the wind has veered towards the NW direction. Two simultaneous phenomena can produce this effect: a horizontal advection of moist air from the sea, which is moved to a layer above the convective boundary layer (around 1500 m), which is mainly driven by the shortwave radiation from the sun. This moist air condensates there and might form scatter cumuli. From this radiosonde data, it is also seen that, at 500 hPa, there is a moist layer that indicates the presence of middle clouds, i.e. altostratus. Such middle clouds can be corroborated from the NOAA satellite images (see Figure 5.24), at 12:12 UTC (note the broken clouds above the Goteborg area). Data from the two channels are presented because they usually complement each other: while IR data (channel 4) have problems in detecting low clouds and fog, the VIS data (channel 2) can be not enough to distinguish thin clouds [82]. At 18:00 UTC, the radiosonde shows a change in the situation: up to 400 hPa the moist layer is well mixed (the difference between T and T_d is kept uniform up to 400 hPa). The NOAA images (see Figure 5.25) show the swedish coast completely covered by a cloud deck. Therefore, the mixing ratio profile is expected to be uniformly decaying, rather than having a relative maximum, as at 12:00 UTC.

To complete the analysis, the mesoscale model MM5 has been used to simulate the situation on the 24th of August 1998. Three nested grid domains are defined with resolutions of 45, 15 and 5 km respectively, centered on the GPS site. The ECMWF analysis are used as boundary conditions and to initialize the model. The topography and land-use have a resolution of 10' ($\approx$ 18.5 km) and a time step for the coarser domain of 100 s. There is no nudging

[‖] As explained in Appendix B, the closer both temperatures are, the closer to saturation the air is.

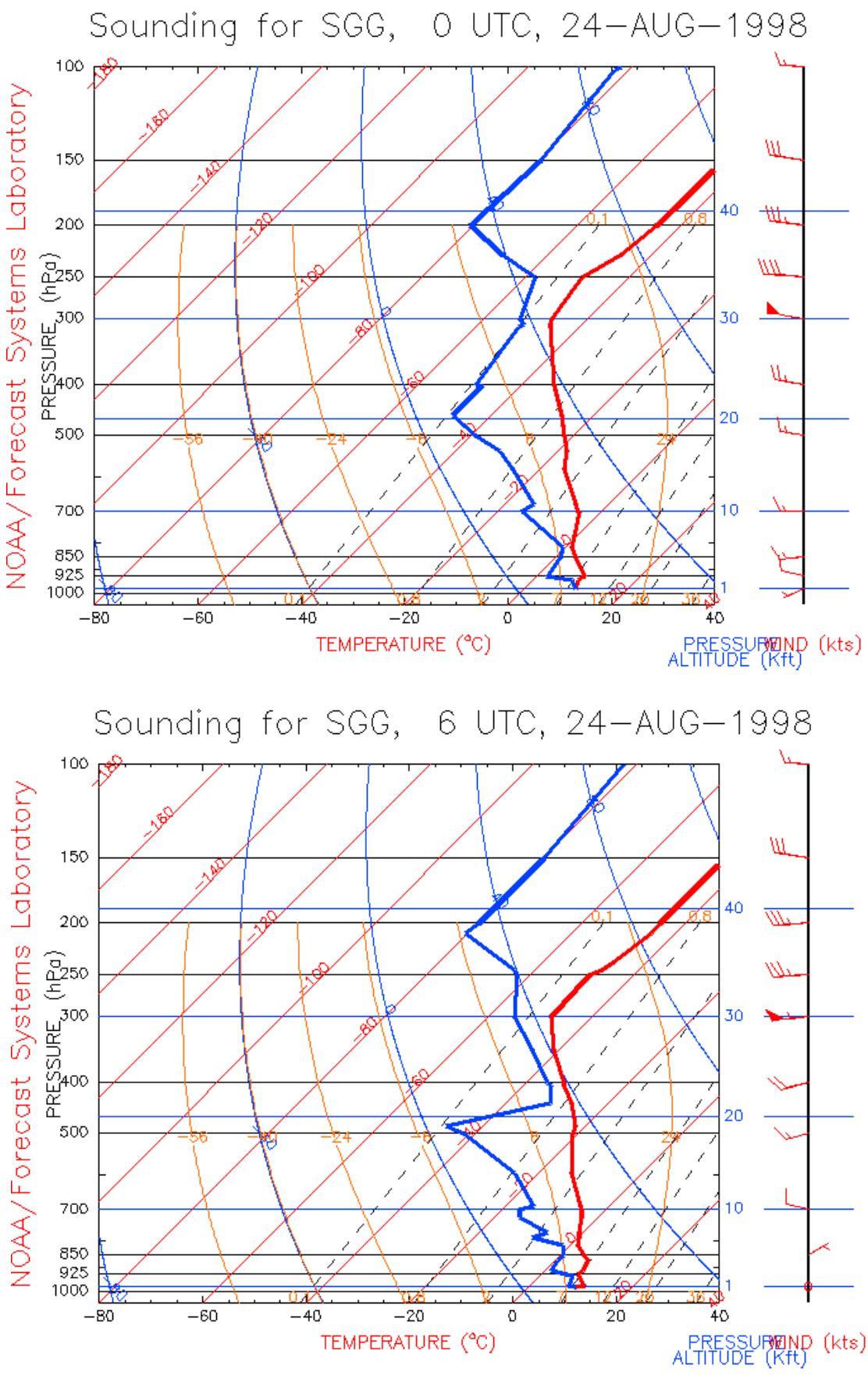

Figure 5.22: Radiosonde data at Goteborg-Landvetter airport (57.67°N, 12.30°E) for 24th August 1998 at 00:00 UTC and 06:00 UTC. Skew-T diagrams represent temperature (red) and dew point temperature (blue). Wind speed and direction is also plotted at each site.

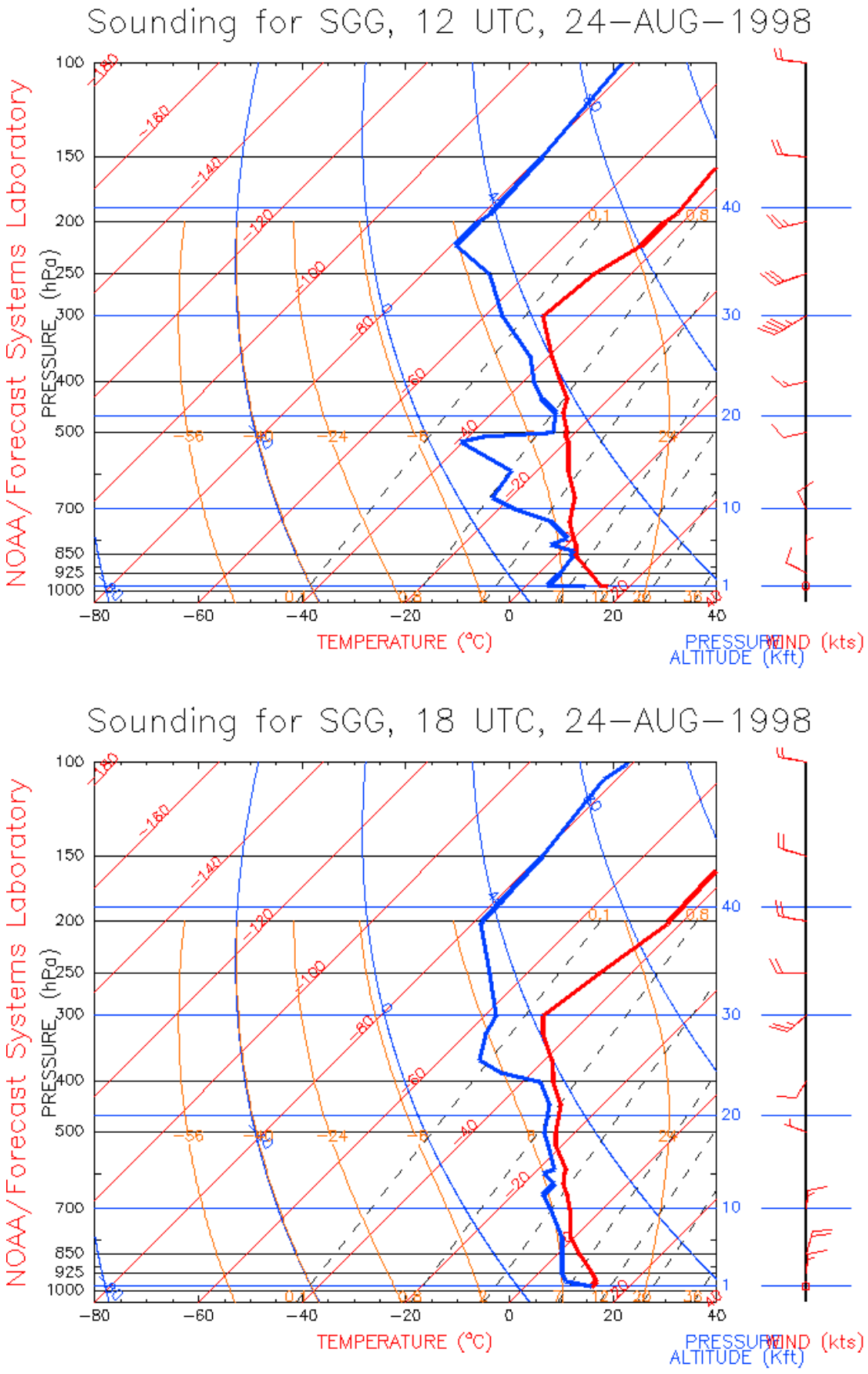

Figure 5.23: Radiosonde data at Goteborg-Landvetter airport (57.67°N, 12.30°E) for 24th August 1998 at 12:00 UTC and 18:00 UTC . Skew-T diagrams represent temperature (red) and dew point temperature (blue). Wind speed and direction is also plotted at each site.

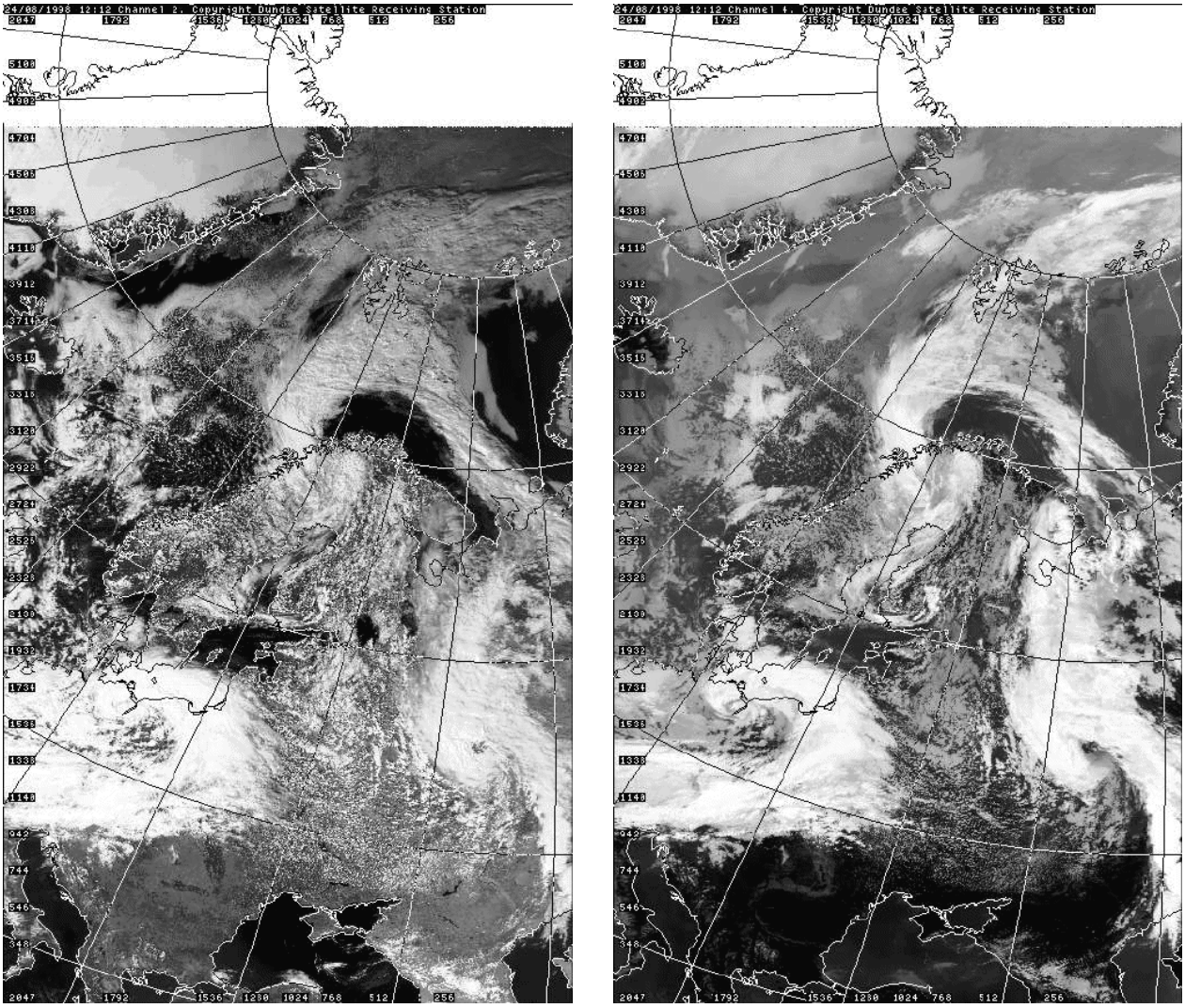

Figure 5.24: NOAA satellite images for channels 2 and 4 at 12:12 UTC.

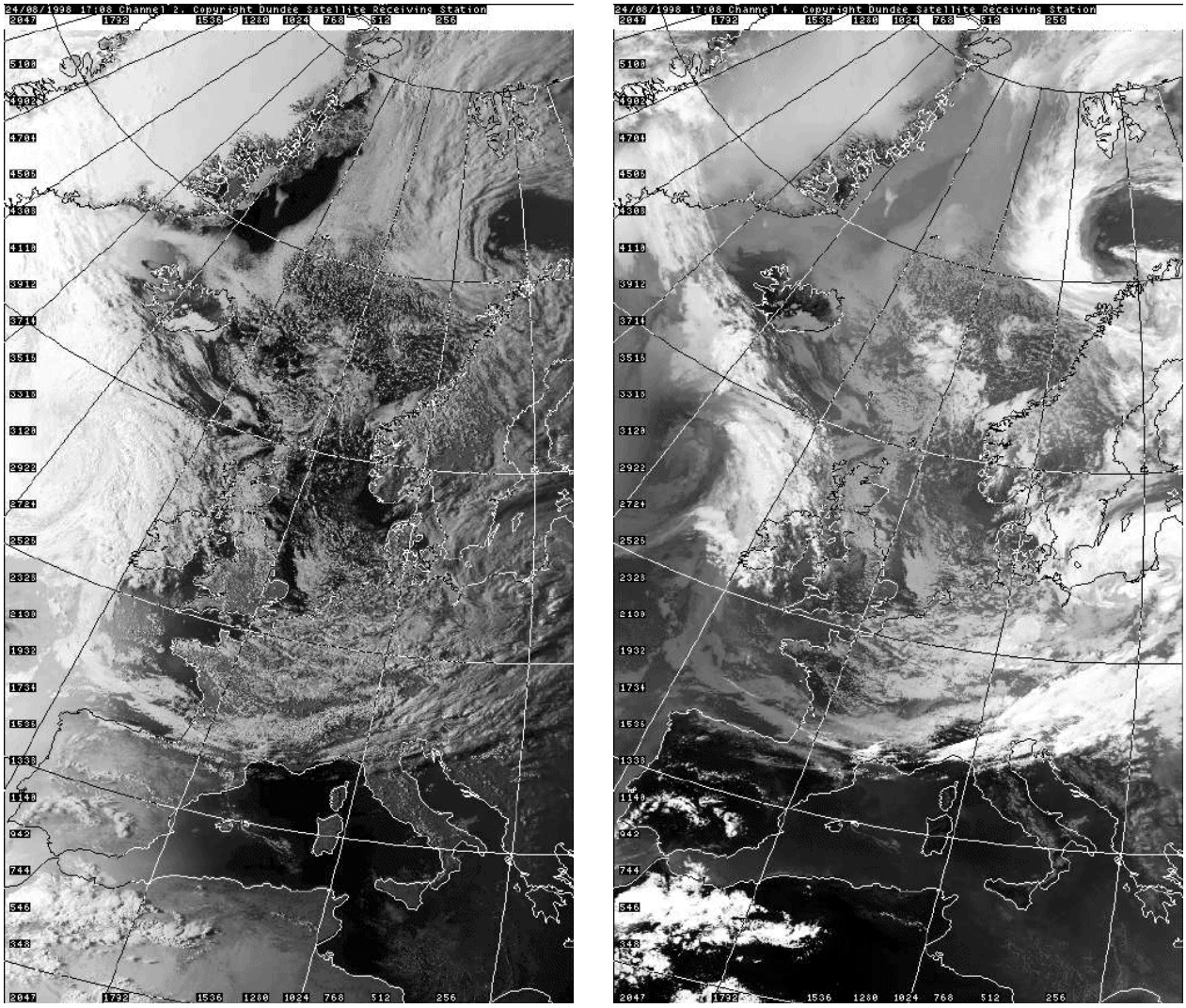

Figure 5.25: NOAA satellite images for channels 2 and 4 at 17:08 UTC.

of surface observations or radiosondes and we will therefore only use the model MM5 to reproduce the general conditions of the region. This analysis provides more information on the meteorological situation which helps in the interpretation of the radiosonde data but the model fails to correctly locate the particular conditions over the GPS network: for instance, the layer close to saturation seen in the radiosonde data at 12:00 UTC over Goteborg is predicted (though not so prominent) at around 1000 m high but 75 km inland, rather than over Goteborg. We therefore use this analysis as a backup.

The model can correctly reproduce the overall evolution of surface pressure at the coarser scale and the wind direction and speed (a predominant NW direction and values lower than 10 m/s). The values of wind speed and direction confirm that the GPS site is influenced by an air mass with sea characteristics and not by the synoptic situation. At the surface level, the evolution of the simulated and measured values of temperature and relative humidity (see Figure 5.26) are similar, though the simulated have a much smoother time-variation. We focus on the third domain (5 km grid) and plot vertical cross-sections along a horizontal line at constant latitude (57.44^o) and longitudes from 11.17^o (80 km in the sea) to 12.38^o (50 km inland) of relative humidity. Between 10 and 12 UTC we observe a strong on shore wind and the formation of saturated layers (rh=100%) around 950 hPa entering from the sea (see Figure 5.27).

The results obtained by the model give a good overview of the phenomena, but they reveal a weakness in their collocation. Furthermore, local and unusual meteorological phenomena like the one here presented are ill-described by the model.

Using all the information gathered and the description given by the model, we can conclude, that the layer closer to saturation that appears at mid-day around 800 hPa is driven by mesoscale and local conditions. It may be explained by the formation of a *Thermal Internal Boundary Layer* (TIBL) where cold and moist air flows (horizontal advection from the sea) over the warm air mass over land (convective TIBL, mainly driven by the shortwave radiation). It is associated in the atmosphere with the horizontal advection of air across a discontinuity at the surface (for instance, the shoreline). This sea-land transition with a flow perpendicular to the shoreline can be sometimes considered as a superposition of a mesoscale, perpendicular to the coast forcing, and a local sea-breeze circulation. Observational studies ([83]) have shown that the condensation level can be reached locally at the top of the TIBL, normally around 1000 m.

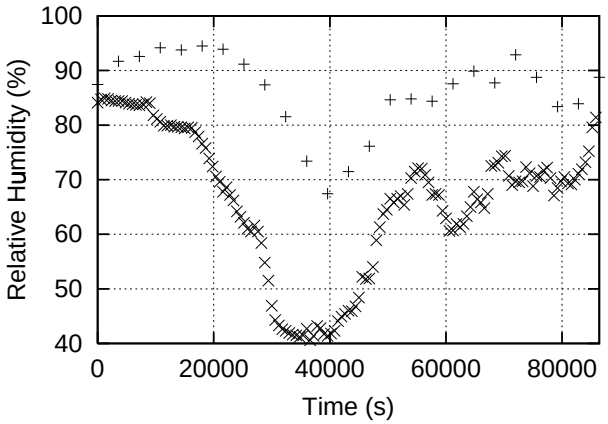
Relative Humidity (%)
100
90
80
70
60
50
40
0
20000
40000
60000
80000
Time (s)

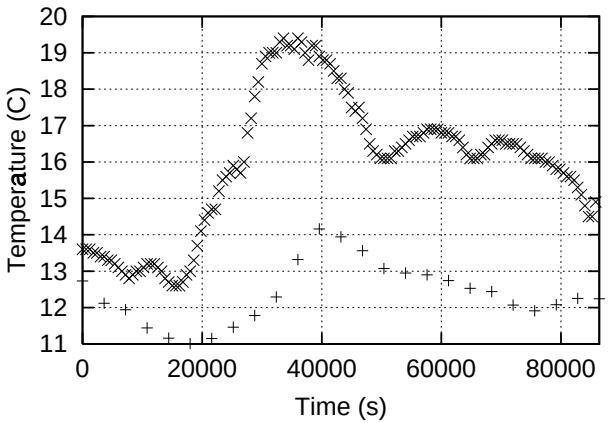
Temperature (C)
20
19
18
17
16
15
14
13
12
11
0
20000
40000
60000
80000
Time (s)

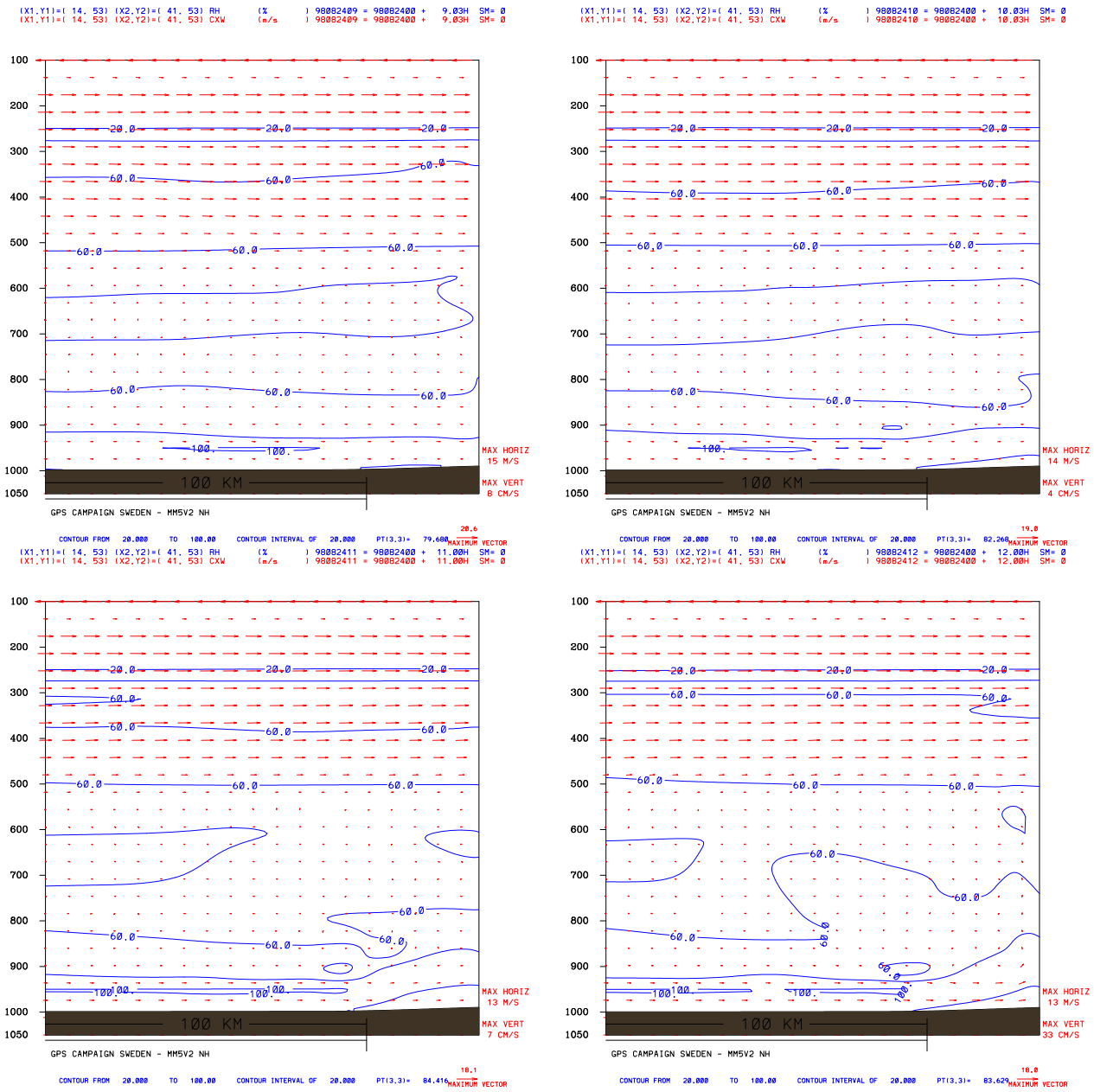

Figure 5.27: MM5 profiles of relative humidity along a line at constant latitude (57.4^o, IGS Onsala site) from longitude 11.17^o (80 km in the sea) to 12.38^o (50 km inland). Profiles are given from left to right and top to bottom, at 09:00 UTC, 10:00 UTC, 11:00 UTC, 12:00 UTC, on August 24, 1998,that is during the phenomena discussed.

5.3.2.4 Verification of the results: A direct comparison of GPS tomography with radiosonde data

Traditional meteorological tools have shown that at around mid-day on August 24, 1998, there was a close-to-saturation layer at 1000 m height, some 40 km north of the GPS network. Radiosonde data from the Goteborg Landvetter airport gave such profile and the meteorological model as well as satellite images provided a description of the meteorological conditions in the area that were consistent with the formation of a TIBL, which is reported in other studies, that leads to a mixing ratio profile with a relative maximum at 1000 m. A more conclusive result of the capabilities of GPS-based tomography is the comparison of vertical profiles obtained for the launch point (north of the IGS site) with the radiosonde data. We have conducted two comparisons: first, directly the wet refractivity obtained through GPS tomography with the refractivity N_w^{rs} computed using the P, T and T_d data from the radiosonde and then applying the following expressions (see Appendix B)

$$r_{rs} = m(P, T_d) = \frac{e_c(T_d)\epsilon}{P - (1-\epsilon)e_c(T_d)} \tag{5.8}$$

$$P_w^{rs} = \frac{P \cdot r_{rs}}{\epsilon} \tag{5.9}$$

$$N_w^{rs}(T, P) = 3.776 \cdot 10^5 P_w^{rs}/T^2 \tag{5.10}$$

where $\epsilon = 0.622$, $e(T_d)$ is the Tetens expression for the mixing ratio ([84]), P_w is the water vapor pressure; second, and a comparison of r_{rs} against r_{tomo} (where rs stands for radiosonde and $tomo$ for tomographic solution), computed through:

$$r_{tomo} = \frac{N_w^{tomo} T^2 \epsilon}{3.776 \cdot 10^5 P} \tag{5.11}$$

(again, P and T are the given by the radiosonde). In order to be consistent with the tomographic procedure, we have averaged the radiosonde data every 400 m. In horizontal, however, there has been no smoothing of radiosonde data; in time, the tomographic solution has also a smoothing constraint given by the Kalman filtering. Results are presented in Figures 5.28 to 5.30 for 12:00 UTC, 18:00 UTC and 24:00 UTC, showing that there is a good agreement of the temporal evolution: at 12:00 UTC both methodologies show a relative maximum of mixing ratio and wet refractivity around 1000 m, though the radiosonde presents a larger value and a wider hump; at 18:00 UTC the saturated layer has disappeared and the profile is in both cases rather uniform. At 24:00 UTC the agreement is good though irregularities are missed in the tomographic reconstruction.

The qualitative and quantitative agreement between both solutions as well as the description inferred from the analysis being consistent with the evolution of the tomographic solution

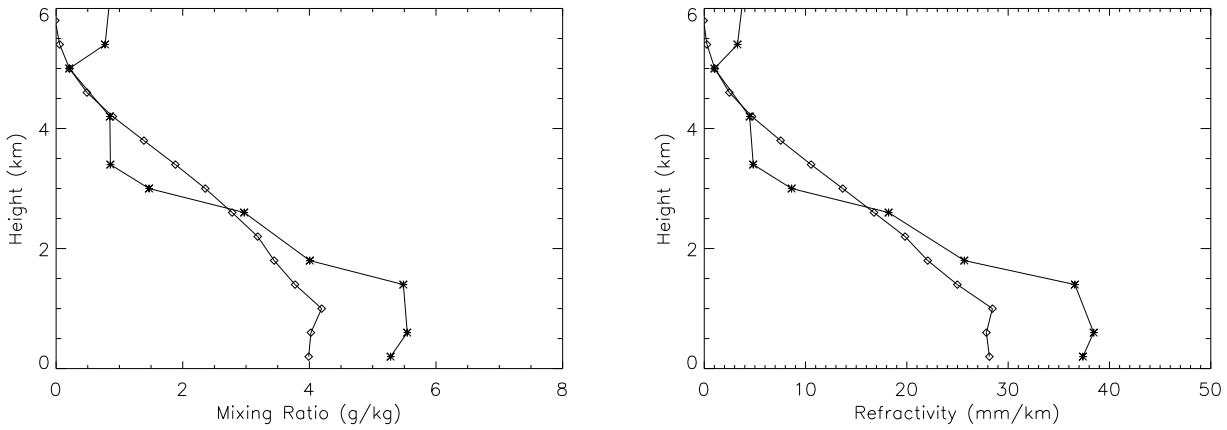

Figure 5.28: Comparison of profiles given by the radiosonde at Goteborg Landvetter airport (asterisks) on August 24 at 12:00 UTC and the vertical profile of tomography for a the location (diamonds) in refractivity (right) and mixing ratio (left).

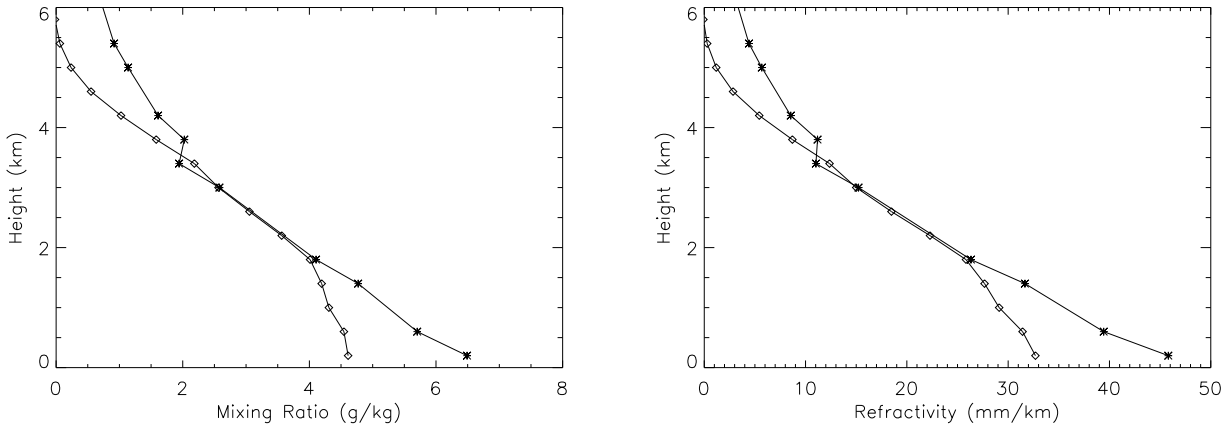

Figure 5.29: Comparison of profiles given by the radiosonde at Goteborg Landvetter airport (asterisks) on August 24 at 18:00 UTC and the vertical profile of tomography for a the location (diamonds) in refractivity (right) and mixing ratio (left).

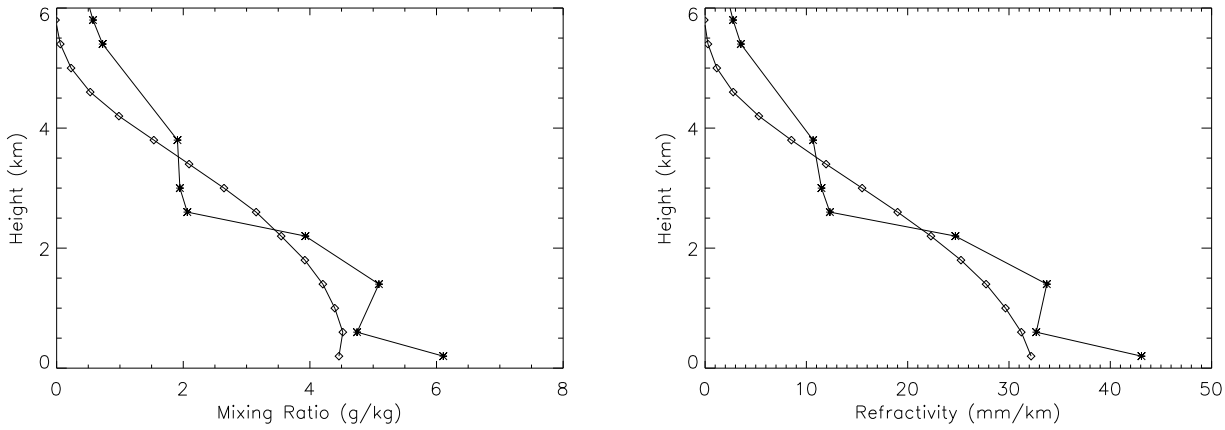

Figure 5.30: Comparison of profiles given by the radiosonde at Goteborg Landvetter airport (asterisks) on August 24 at 24:00 UTC and the vertical profile of tomography for a the location (diamonds) in refractivity (right) and mixing ratio (left). Note that the irregularities and 1500 m are sensed in the tomographic solution, though much smoother.

show that tomography is providing accurate spatio-temporal structures. The level of agreement of this experiment cannot be conclusive, given the reduced number of stations and the availability of surface pressure measurements from one site only.

5.3.2.5 Verification of the results: Comparison for August 29, 1998 data

As a second example of the GPS tropospheric tomography capabilities, we processed data from a day in which no particular features where seen in the time-series of zenith delays and gradients. We selected August, 29 for that purpose. The tomographic approach followed the same parameters as for August 24 and the radiosonde data from Landvetter airport were used for comparison. Results for 12:00 UTC and 18:00 UTC are presented in Figures 5.31 and 5.32 for wet refractivity and mixing ratio. Note that profiles are in very good agreement and at 12:00 UTC the small relative maximum at 1200 m is clearly visible in the solutions for both methodologies. As expected, the values for the lowest layers are smaller for the tomographic solution. This is due to the fact that very few rays sense the lower voxels at long distances (the airport is 37 km from the IGS site) and therefore solution for those voxels is mainly driven by the smoothing constraints, taking information from other voxels.

The meteorological analysis for August 29 has not been made because the date is taken as a reference to show the consistency of the agreement for different conditions.

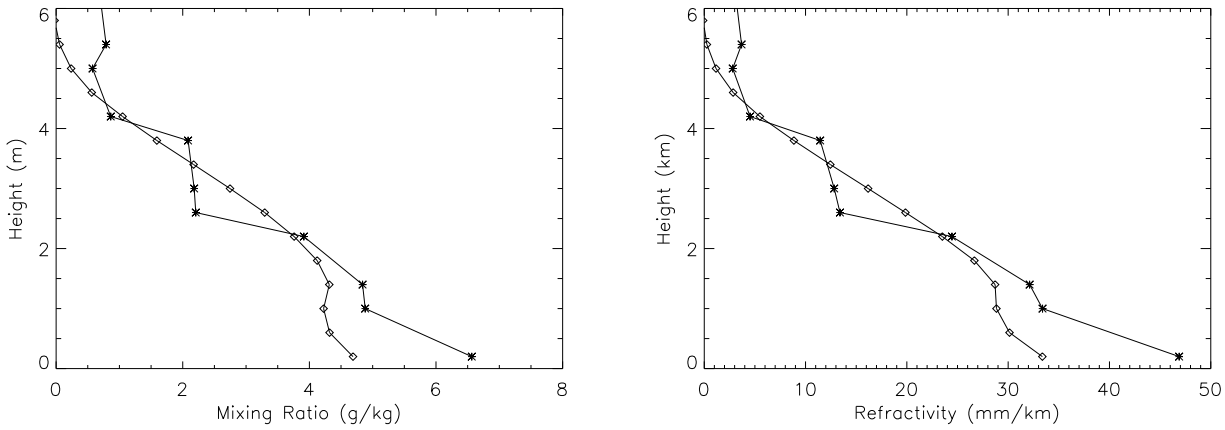

Figure 5.31: Comparison of profiles given by the radiosonde at Goteborg Landvetter airport (asterisks) on August 29 at 12:00 UTC and the vertical profile of tomography for a the location (diamonds) in refractivity (right) and mixing ratio (left).

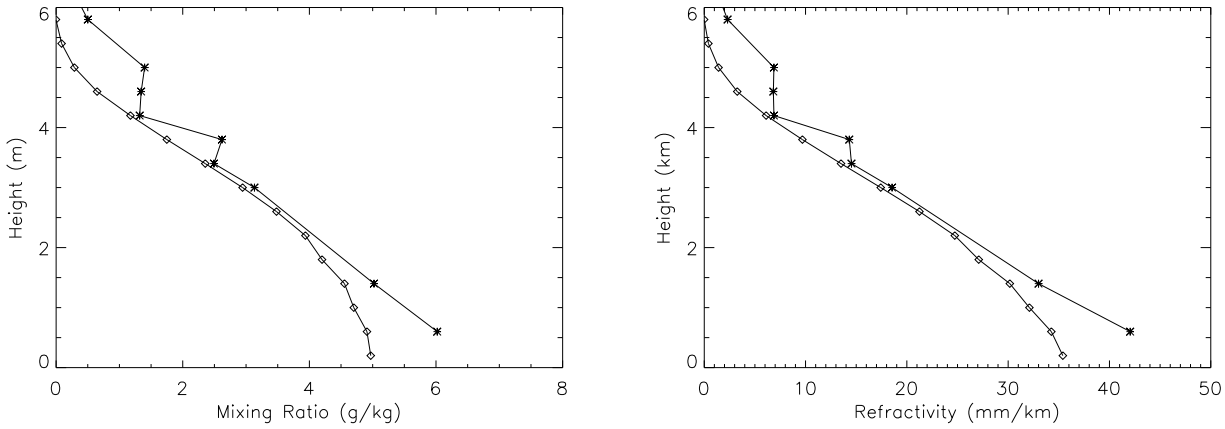

Figure 5.32: Comparison of profiles given by the radiosonde at Goteborg Landvetter airport (asterisks) on August 29 at 18:00 UTC and the vertical profile of tomography for a the location (diamonds) in refractivity (right) and mixing ratio (left).

5.3.2.6 Conclusions on the REGINA experiment

A complex meteorological situation characterized by a saturated layer at the top of the boundary layer has been successfully analyzed using GPS tomography. The complexity is due to the combination of spatial scales associated with the horizontal advection of moist sea air (mesoscale process) and the formation of a convective boundary layer around noon (local scales). The 4D tomographic fields have been verified using other meteorological tools. In particular, we have used the numerical model MM5 and radiosonde data; the former did not correctly predict the radiosonde observations but it provided the background information to understand the meteorological situation; radiosonde data were used for comparison with the tomographic fields.

Radiosonde and tomographic data show a very good spatial and temporal agreement. The particular feature of the saturated layer on top of the boundary layer (at around 1000 m height) is clearly depicted in both methods.

A second date, August 29, has been selected to show the consistency of the agreement for a different meteorological situation.

The agreement is a strong evidence that tropospheric tomography using ground GPS stations is feasible, and that more ambitious campaigns with deployment of many more stations, in a geometry suitable for tomography, as well as having traditional meteorological measurements sensing the same area, will in the near future yield a much better agreement of results.

It is clear that by properly ingesting GPS measurements into the mesoscale models such as MM5, meteorological phenomena which normally are poorly represented in the models can be taken into account (some of such phenomena were described above: interactions of sea and land air masses, formation of convective boundary layers and the evolution of broken cumuli). Weather predictions can largely benefit from the assimilation of GPS data into the models.

The quantitative differences shown in the comparison are due to the particular characteristics of each methodology. Radiosondes provide a punctual sounding of the atmosphere, representing very local meteorological magnitudes. The REGINA campaign, used for GPS-based tomography, consisted of only 7 stations. Constraints in tomography have played an important role to fill the information gap (as compared with e.g. the Hawaii 1997 data). Furthermore, the stations are located about 40 km away from the radiosonde launch site and therefore the GPS stations are not directly sensing the same area, but via the slant paths.